Numerical validation of isotropic and transversely isotropic constitutive models for healthy and unhealthy cerebral arterial tissues

P. Tricerri, L. Dedè, A. Quarteroni, A. Sequeira

Numerical validation of isotropic and transversely isotropic constitutive models for healthy and unhealthy cerebral arterial tissues

Paolo Tricerri[1,2*,†] Luca Dedè[1], Alfio Quarteroni[1,3], Adélia Sequeira[2]

[1] Chair of Modeling and Scientific Computing, École Polytechnique Fédérale de Lausanne,
Av. Piccard, Station 8, CH-1015 Lausanne, Switzerland

[2] Department of Mathematics and CEMAT, Instituto Superior Técnico, University of Lisbon,
Av. Rovisco Pais 1, 1049-001 Lisbon, Portugal

[3] MOX - Modeling and Scientific Computing, Dipartimento di Matematica "F. Brioschi", Politecnico di Milano,
via Bonardi 9, 20133 Milano, Italy (on leave)

19th December 2013

Abstract

This paper deals with the validation of constitutive models for healthy and unhealthy cerebral arterial tissues by means of numerical simulations of static inflation tests on a cylindrical geometry representing a specimen of anterior cerebral artery. The healthy arterial tissue is described by means of isotropic and transversely isotropic models. In particular, we validate a transversely isotropic multi-mechanism law, specifically proposed for the cerebral arterial tissue, for which the recruitment of the collagen fibers occurs at finite strains. Moreover, we consider numerical simulations of unhealthy cerebral arterial tissues by taking into account the mechanical weakening of the vessel wall that occurs during early development stages of cerebral aneurysms. We study the effects of the mechanical degradation on kinematic quantities of interest, namely the stresses distribution, that are commonly related to the progressive degradation of the arterial tissue by simulating static inflation tests for both isotropic and transversely isotropic models, including the multi-mechanism law.

Key words: cerebral arterial tissue; hyperelastic isotropic models; hyperelastic transversely isotropic models; multi-mechanism; mechanical weakening; finite elements.

1 Introduction

The normal function of the brain's control centers is dependent upon adequate supply of oxygen and nutrients through a dense network of arteries establishing the cerebral blood circulation. However, the proper function of cerebral arteries may be disrupted by injuries caused by trauma or by the occurrence of other cerebrovascular accidents (e.g. stroke or vasospasm) resulting from the development of cardiovascular diseases as cerebral aneurysms. In the latter case, efforts to better understand the disease process require, among the different aspects, the characterization of the mechanical response of the cerebral arteries to several hemodynamical factors. In this respect, the definition of proper mathematical models based on the knowledge of the vessel properties represents a critical step toward the enhanced understanding of cardiovascular diseases.

---

*Corresponding author: Paolo Tricerri, CMCS-MATHICSE-SB, École Polytechnique Fédérale de Lausanne, Av. Piccard, Station 8, CH-1015 Lausanne, Switzerland

†E-mail: paolo.tricerri@epfl.ch

As other blood vessels, cerebral arteries consist of three main concentric layers of material [1] of which the innermost is the tunica intima, the middle one is the tunica media, and the outermost is the tunica adventitia; in addition, the tunica intima and the media are separated by the internal elastic lamina. In healthy arteries, the tunica media and the tunica adventitia are the main responsible of the overall mechanical properties of the tissue, being the contribution provided by the tunica intima negligible [2]. The passive mechanical properties of the media and adventitia are determined by those of their two main constituents: the elastin and collagen fibers [2, 3]. The typical mechanical behavior of healthy arteries is highly nonlinear and anisotropic with a stiffening effect occurring at high stresses [1, 4, 5]; such effect is due to the recruitment of the collagen fibers embedded in the elastin network of the media and adventitia layers. This paper is concerned with the numerical validation of isotropic and transversely isotropic mathematical models for the description of the in vitro passive mechanical behavior of healthy cerebral arteries; in vivo effects as perivascular tissue and active contraction of the arterial tissue are not considered in this study. As discussed in [3], several mathematical models have been proposed for biological tissues, in particular blood vessels [6, 7]. Among these, most of the constitutive laws describe the vessel wall, at the macroscopic scale, as a continuous body whose mechanical behavior is modeled according to the finite elasticity theory [2, 3, 6, 8]. The most common constitutive laws are of phenomenological type, for which isotropic models represent the artery as a single layer material [6, 9]. Isotropic constitutive laws are largely used to model the arterial tissue due to their simplicity and the limited number of material parameters that usually need to be estimated for characterizing the mechanical response. For instance, the Mooney-Rivlin and the neo hookean models have been largely used in literature to describe the arterial tissue [10, 11, 12, 13, 14]. However, they turned out to be inappropriate to fit the experimental data considered in this work [15]. For that reason in this paper we use isotropic laws based on the St. Venant-Kirchhoff [8] and exponential type models [9].

Based on the experimental observations of the anisotropic mechanical response of the arterial tissue, since the seminal work in [2], several anisotropic models have been formulated to include in the constitutive laws the mechanical contribution of the collagen fibers. Such models rely on the mechanical theory of fiber-reinforced composites [16] for which the tissue is assumed to be composed by a single layer embedding two constituents: the so called background material (whose main constituent is the elastin) and the fibrous network (i.e. the collagen fibers) which endows the tissue with its anisotropic response to external loads. The mechanical response of the background material is usually described by isotropic models, while the mechanical contribution of the collagen fibers is represented by a finite number of fiber families [17, 18, 19, 20, 21], each of them oriented along a characteristic direction for the tissue at rest. In this work, the recruitment of the collagen fibers is supposed to occur either at zero strains [17, 20], or at finite strains [21, 22], yielding the so called multi-mechanism constitutive law. We remark that the multi-mechanism model in [21, 22] was specifically proposed after the analysis of the experimental measurements reported in [15]; for this reason we consider this set of data. However, other studies have focused either on the characterization of the mechanical behavior of cerebral arteries by considering inflation-extension tests [23] or on the mechanical properties of other arteries (e.g. [24, 25]).

The arterial tissue behaves as a nearly incompressible material within the physiological range of deformations. We enforce the nearly incompressibility constraint by penalizing the deformations of the tissue leading to changes in its volume for which we employ the approach based on the multiplicative decomposition of deformation tensor into a volumetric and an isochoric part [26, 27]. The numerical validation of the constitutive models is carried out by means of finite elements simulations of static inflation tests on a computational domain representing a specimen of anterior cerebral artery for which experimental measurements of the strain-stress relation are provided in [15].

Afterwards, we consider the mathematical modeling and numerical simulations of unhealthy cerebral arterial tissue. Cardiovascular diseases such as cerebral aneurysms are related to degenerative changes in the mechanical properties of the vessel wall driven by a complex interaction of biological and hemodynamic factors. The understanding of the onset and the growth of cerebral aneurysms is still subject of debate, but it is generally accepted that unphysiological hemodynamic forces (e.g. high wall shear stress [28]) play a key role, in concomitance with genetic factors ([29]) and structural features of the cerebral arterial tissue ([30, 31, 32]). More specifically, as described in [15, 28, 30, 33, 34, 35], during the onset of a cerebral

aneurysm, the internal elastic lamina and the elastin network in the tunica media become markedly degraded or fragmented. Indeed, the transition from the parent vessel [30] to aneurysm is characterized by a sharp break in the media layer [31, 34]. Moreover, it has been observed in [36] that the tissue composing the dome of a cerebral aneurysm [3] consists primarily of collagen fibers, while the elastin tends to be fragmented or absent; in addition, the aneurysm growth involves a significant remodeling of the collagen fibers in the dome [7, 37]. In this work, the weakening of the arterial tissue that occurs in diseased states of arteries, as in the early stages formation of a cerebral aneurysm, is described by means of an isotropic weakening model for the background material (elastin). According to the approach proposed in [38], the level of mechanical weakening of the tissue is introduced in the constitutive model for healthy cerebral arterial tissue by means of a dimensionless parameter $D \in [0, 1)$. We consider different levels of mechanical weakening of the arterial tissue prescribing a priori different values of D in the constitutive models. The influence of the modeling choice on the deformations and stresses distribution throughout the body during static inflation tests is studied for the different levels of mechanical weakening.

The paper is organized as follows. Section 2 introduces the kinematics quantities for the formulation of the constitutive laws and presents the mathematical models used to describe the healthy cerebral arterial tissue; in addition, the weakening model for the arterial tissue is presented. Section 3 deals with the finite element approximation of the linear momentum equation governing the deformations of the tissue under the action of external forces. The numerical results are presented and discussed in Section 4. Conclusions follow in Section 5.

2 Mathematical modeling of the arterial tissue

This section deals with the mathematical modeling of the arterial tissue by taking into account the macroscopic nature of the vessel wall. Sec. 2.1 introduces the basic notations used to describe the motion of a continuous body under the action of external forces. Sec. 2.2 presents the mathematical models for the description of the healthy cerebral arterial tissue. Sec. 2.3 focuses on the description of the experimental data fitting procedure for estimating the material parameters of the constitutive laws. Sec. 2.4 deals with the mathematical modeling of unhealthy arterial tissue. In Sec. 2.5 we describe the choice of the weakening parameter D for the comparisons of different constitutive models representing unhealthy cerebral arterial tissues.

2.1 Kinematics of continuous media

The arterial tissue is assumed to be a continuous medium (also referred as continuous body) whose elastic properties are represented by suitable mathematical models. The kinematics of the vessel wall is described in terms of the vectorial and tensorial fields defined for the continuum theory [8]; the constitutive models (laws) are formulated under the finite elasticity assumption [3].

Let $\mathcal{B}_0 \subset \mathbb{R}^3$ and $\mathcal{B} \subset \mathbb{R}^3$ be the reference and current configuration of a continuous body, respectively. The position of a point in $\mathcal{B}_0$ is indicated by the material coordinates $\boldsymbol{X}$, while, in the current configuration, by the spatial coordinates $\boldsymbol{x}$. The motion from $\mathcal{B}_0$ to $\mathcal{B}$ experienced by the body under the action of external forces is described by the nonlinear function $\phi(\boldsymbol{X}, t)$ that maps any point $\boldsymbol{X} \in \mathcal{B}_0$ into the point $\boldsymbol{x} \in \mathcal{B}$ at each time $t \in \mathbb{R}_+$. The material (i.e. Lagrangian) description of the displacement at each point $\boldsymbol{X} \in \mathcal{B}_0$ is represented by the vector $\boldsymbol{d}(\boldsymbol{X}) = \boldsymbol{x} - \boldsymbol{X} \in \mathbb{R}^3$. Locally, the deformations of the body in the material coordinates are described by the deformation gradient tensor $\boldsymbol{F}$, the local volume ratio J (also referred as Jacobian) and the right Cauchy-Green tensor $\boldsymbol{C}$ defined as:

$$\boldsymbol{F} = \nabla_{\boldsymbol{X}} \phi = \nabla_{\boldsymbol{X}} \boldsymbol{d} + \boldsymbol{I}, \qquad J = \det(\boldsymbol{F}) > 0, \qquad \text{and} \qquad \boldsymbol{C} = \boldsymbol{F}^T \boldsymbol{F}, \tag{1}$$

respectively; $\nabla_{\boldsymbol{X}} \boldsymbol{d}$ is the material gradient of the displacement field and $\boldsymbol{I}$ is the second order identity tensor in $\mathbb{R}^3$ [8]. We focus on the mathematical modeling of the passive mechanical response of the arterial tissue which is assumed to be an hyperelastic material whose mechanical behavior is characterized by means of a

3

(a) Reference configuration $\mathcal{B}_0$

(b) Cross section of $\mathcal{B}_0$. $\Delta P = p_{in} - p_{out}$, $p_{out} = 0$.
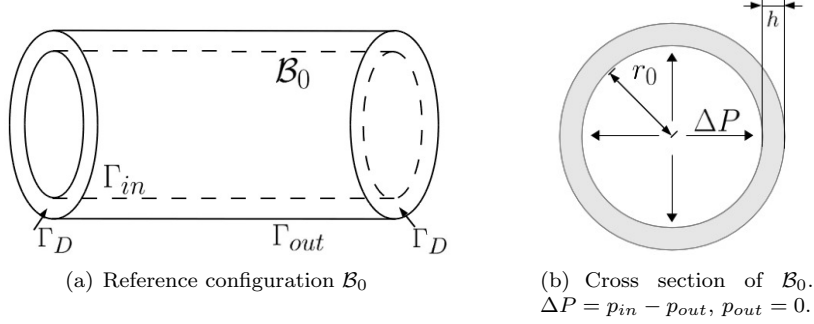
Figure 1: Computational domain $\mathcal{B}_0$ representing the arterial specimen and data of problem (3).

scalar-valued function of the deformations (measured either by $\boldsymbol{F}$ or $\boldsymbol{C}$), the so called strain energy function $\mathcal{W}$ [8]. The stresses that occur in the body during its motion are measured in both the reference and current configuration through the first Piola-Kirchhoff tensor $\boldsymbol{P}$ and the Cauchy stress tensor $\boldsymbol{\sigma}$ defined, respectively, as:

$$\boldsymbol{P} = \frac{\partial \mathcal{W}}{\partial \boldsymbol{F}} \qquad \text{and} \qquad \boldsymbol{\sigma} = \frac{1}{J} \boldsymbol{P} \boldsymbol{F}^T. \tag{2}$$

The mechanical response of the body to external loads is governed by the linear momentum equation in Lagrangian form complemented by suitable boundary conditions. Since in this work we specifically consider inflation tests on cylindrical specimen of arteries, the mechanical problem is defined in the computational domain $\mathcal{B}_0$ of Fig. 1(a) that represents a cylindrical geometry of internal radius r_0 and thickness h (as in Fig. 1(b)). The problem reads:

$$\text{find} \quad \boldsymbol{d} : \mathcal{B}_0 \to \mathbb{R}^3 \quad : \quad \begin{cases} \text{Div}(\boldsymbol{P}(\boldsymbol{d})) = \boldsymbol{0} & \text{in } \mathcal{B}_0, \\ \boldsymbol{P}\boldsymbol{n} = -p_{out}\boldsymbol{n} & \text{on } \Gamma_{out}, \\ \boldsymbol{P}\boldsymbol{n} = -p_{in}\boldsymbol{n} & \text{on } \Gamma_{in}, \\ \boldsymbol{d} = \boldsymbol{0} & \text{on } \Gamma_D, \end{cases} \tag{3}$$

where Γ_D is the subset of $\partial\mathcal{B}_0$ where homogeneous Dirichlet boundary conditions are imposed; the subsets Γ_{out} and Γ_{in} indicate the external and internal surfaces of the body and $\boldsymbol{n}$ is the outward directed, unit vector normal to the corresponding surface. p_{out} and p_{in} represent the pressures acting on Γ_{out} and Γ_{in} defining the transmural pressure $\Delta P = p_{in} - p_{out}$. We assume, for simplicity, that $p_{out} = 0$, thus yielding $\Delta P = p_{in}$ (see Fig. 1(b)). The undeformed internal radius ($r_0 = 0.033$ cm) and the vessel wall thickness ($h = 0.010$ cm) of the tissue represented in Fig. 1(b) correspond to the physiological dimensions of the anterior cerebral artery described in [15, 22]. We set the length L of the cylindrical specimen $L = 2$. The range of transmural pressures considered to validate the different constitutive models is the physiological one occurring in cerebral arteries during one heart beat; therefore, $\Delta P \in [70, 150]$ mmHg [39].

The arterial tissue behaves as a nearly incompressible material within the physiological range of deformations [40]. In order to model such behavior, we adopt the approach based on the volumetric-isochoric split of the deformation gradient tensor $\boldsymbol{F}$ [26, 27] which has been used in literature (e.g. [13, 19, 41, 42]) for numerical simulations of the arterial tissue. According to [26], the local deformation gradient $\boldsymbol{F}$ and the right Cauchy-Green $\boldsymbol{C}$ tensors are split into a so called volumetric and an isochoric part by means of the relations:

$$\boldsymbol{F} = \left(J^{1/3}\boldsymbol{I}\right)\overline{\boldsymbol{F}} \quad \text{and} \quad \boldsymbol{C} = \left(J^{2/3}\boldsymbol{I}\right)\overline{\boldsymbol{C}}, \tag{4}$$

where the tensors $J^{1/3}\boldsymbol{I}$ and $J^{2/3}\boldsymbol{I}$ are associated with isotropic volume-changing deformations, while the tensors $\overline{\boldsymbol{F}} := J^{-1/3}\boldsymbol{F}$ and $\overline{\boldsymbol{C}} := J^{-2/3}\boldsymbol{C}$ with volume-preserving deformations of the material, for which $\det(\overline{\boldsymbol{F}}) \equiv \det(\overline{\boldsymbol{C}}) \equiv 1$. Based on this kinematic assumption, the strain energy function $\mathcal{W}$ can be reformulated in its penalty form as:

$$\mathcal{W} = \mathcal{W}(\boldsymbol{C}, J) = \mathcal{U}(J) + \overline{\mathcal{W}}(\overline{\boldsymbol{C}}), \tag{5}$$

4

where the volumetric term $\mathcal{U}(J)$ penalizes the volume-changing deformations and the isochoric part $\overline{\mathcal{W}}(\overline{C})$ characterizes the mechanical response of the material to external loads according to different constitutive laws. The first Piola-Kirchhoff tensor P is defined according to Eq. (2) as:

$$P = \widetilde{P} + \overline{P} = \frac{\partial \mathcal{U}(J)}{\partial F} + \frac{\partial \overline{\mathcal{W}}(\overline{C})}{\partial F}, \tag{6}$$

where $\widetilde{P}$ and $\overline{P}$ measure the stresses due to volume-changing and isochoric deformations, respectively. We remark that, in order to guarantee the existence of realistic physical solutions of Eq. (3), the strain energy function in Eq. (5) has to satisfy the polyconvexity condition (see [43, 44]). In addition, both the functions $\mathcal{U}(J)$ and $\overline{\mathcal{W}}(\overline{C})$ must satisfy the requirement of objectivity under changes of coordinates systems [8]. We discuss the choice of $\mathcal{U}$ and $\overline{\mathcal{W}}$ in Secs. 2.2.1 and 2.2.2.

2.2 Volumetric and isochoric strain energy functions for the arterial tissue

2.2.1 The choice of the volumetric strain energy function $\mathcal{U}$

Due to the polyconvexity requirements on the strain energy function $\mathcal{W}$, the volumetric term $\mathcal{U} = \mathcal{U}(J)$ must be a strictly convex function of J endowed with a unique minimum in $J = 1$ [8]. This component of the strain energy function $\mathcal{W}$ can be chosen independently from the isochoric term $\overline{\mathcal{W}}$ of Eq. (5), even if the decomposition approach is effective only when the functions $\mathcal{U}$ and $\overline{\mathcal{W}}$ are properly balanced.

Different functions $\mathcal{U}$ have been proposed in literature (see for instance [27, 45, 46]); in this work, it is assumed in the form:

$$\mathcal{U}(J) = \frac{\kappa}{4}\left[(J-1)^2 + \log^2 J\right], \tag{7}$$

in order to penalize the cases $J \neq 1$ and $J \rightarrow 0$ corresponding to unphysical solutions. The parameter κ, which can be interpreted as a bulk modulus, assumes the role of a user-specified penalty parameter that is suitably determined to weakly enforce the nearly incompressible response of the material in the physiological range of deformations of the body. The choice of the parameter κ is a trade-off between the need to represent the quasi-incompressible behavior of the tissue and to yield a physical meaningful displacement of the body.

2.2.2 The choice of the isochoric strain energy function $\overline{\mathcal{W}}$

We consider the healthy arterial tissue as a homogeneous body with constant material parameters for which the layered structure of the vessel wall is neglected. As described in [1], the arteries show a highly nonlinear and anisotropic mechanical behavior. In the last decades, structurally motivated models (as for instance transversely isotropic laws), that take into account the fibrous nature of the tissue into the constitutive relation, have been proposed and used in order to represent the anisotropic behavior of arteries [2, 21, 47]. However, isotropic models are still largely used to represent the arterial tissue [2, 3, 6]. For this reason, we will consider both isotropic and transversely isotropic models. We remark that, in order for the strain energy function $\mathcal{W}$ to satisfy the polyconvexity condition for all the deformations of the body, also the isochoric strain energy function $\overline{\mathcal{W}}$ must be a polyconvex function for all states of deformations.

2.2.3 Isotropic constitutive models

When the arterial tissue is modeled by means of isotropic models, it is assumed to be composed by a unique elastic material by neglecting its fibrous nature. Due to requirements of frame indifference of the constitutive law [8], the isochoric part of the strain energy function in Eq. (5), indicated as $\overline{\mathcal{W}}_{iso}$, is formulated in terms of the principal invariants of $\overline{C}$, as:

$$\overline{\mathcal{W}}_{iso} = \overline{\mathcal{W}}_{iso}(\overline{C}) = \overline{\mathcal{W}}_{iso}(\overline{I}_1, \overline{I}_2, \overline{I}_3) = \overline{\mathcal{W}}_{iso}(\overline{I}_1, \overline{I}_2), \tag{8}$$

5

where:

$$\overline{I}_1 = \text{Tr}(\overline{\boldsymbol{C}}) = J^{-2/3}I_1, \quad \overline{I}_2 = \frac{1}{2}\left[\text{Tr}^2(\overline{\boldsymbol{C}}) - \text{Tr}(\overline{\boldsymbol{C}}^2)\right] = J^{-4/3}I_2 \quad , \text{ and } \quad \overline{I}_3 = \det(\overline{\boldsymbol{C}}) = J^{-2}I_3, \quad (9)$$

with (I_1, I_2, I_3) the principal invariants of $\boldsymbol{C}$ [8]. We remark that the explicit dependency of $\overline{\mathcal{W}}_{iso}$ on $\overline{I}_3$ in Eq. (8) can be dropped since $\overline{I}_3 \equiv 1$, due to the definition of the isochoric right Cauchy-Green tensor $\overline{\boldsymbol{C}}$.

A common constitutive model is the St. Venant-Kirchhoff (SVK) [8], for which:

$$\overline{\mathcal{W}}_{iso} = \overline{\mathcal{W}}_{iso}^{SVK}\left(\overline{I}_1, \overline{I}_2\right) = \left(\frac{\lambda}{8} + \frac{\mu}{4}\right)\overline{I}_1^2 - \left(\frac{3}{4}\lambda + \frac{\mu}{2}\right)\overline{I}_1 - \frac{\mu}{2}\overline{I}_2 + \frac{9}{8}\lambda + \frac{3}{4}\mu, \quad (10)$$

where λ and μ are the Lamé parameters, depending on the Young modulus E and Poisson's ratio ν as:

$$\lambda = \frac{E\nu}{(1+\nu)(1-2\nu)} \qquad \text{and} \qquad \mu = \frac{E}{2(1+\nu)}. \quad (11)$$

We recall that the Young modulus measures the mechanical stiffness of the material and the Poisson's ratio $\nu \in (0, 0.5)$ represents the relative change of volume of an elementary cube inside the body due to deformations of the material. We remark that the incompressibility constraint is yielded for $\nu \to 0.5$.

In addition, we consider the first order exponential (EXP1) model proposed in [9], for which:

$$\overline{\mathcal{W}}_{iso} = \overline{\mathcal{W}}_{iso}^{EXP1}(\overline{I}_1) = \frac{\alpha_1}{2\gamma_1}\left(e^{\gamma_1(\overline{I}_1 - 3)} - 1\right) \quad (12)$$

and the second order exponential model (EXP2) [44]:

$$\overline{\mathcal{W}}_{iso} = \overline{\mathcal{W}}_{iso}^{EXP2}(\overline{I}_1) = \frac{\alpha_2}{2\gamma_2}\left(e^{\gamma_2(\overline{I}_1 - 3)^2} - 1\right), \quad (13)$$

where $\alpha_1, \alpha_2, \gamma_1$ and γ_2 are suitable material parameters. In Eqs. (12) and (13) α_1 and α_2 measure the mechanical stiffness of the arterial tissue, while γ_1 and γ_2 are representative of the level of nonlinearity of the mechanical response of the vessel wall.

We remark that the strain energy functions associated to the exponential (EXP1 and EXP2) models of Eqs. (12) and (13) satisfy the polyconvexity condition for all the states of deformations [44]. Conversely, the SVK model does not satisfy this condition under compression states of deformations [8, 48]; however, we observe that this situation does not occur during inflation tests of cylindrical geometries like the one represented in Fig. 1(a). We remark that the SVK constitutive model, and eventually its linearized approximation are often used in literature to model the arterial tissue [10, 11, 42, 49, 50]; for this reason, we will include the SVK model for a numerical comparison.

2.2.4 Transversely isotropic constitutive model

When modeling the passive mechanical response of the vessel wall by means of transversely isotropic models, the tissue is assumed to be composed of an isotropic medium, also called background material, in which a network of collagen fibers is immersed [2, 3]. Such models describe the overall mechanical behavior of the arterial tissue as the sum of the contributions provided by its two main constituents. Based on experimental observations, the two constituents are the elastin and the collagen fibers respectively, that are the main components of the vessel wall [1, 2]. In literature (see [39, 44] and references therein) the transversely isotropic models that are commonly employed are based on the theory of fiber-reinforced composites [16]. The contribution of the collagen fibers to the overall mechanical behavior of the tissue is usually modeled as the sum of the mechanical responses of a finite number of families of collagen fibers. As described in [21, 22], the collagen fibers contribute to the mechanical response of the arterial tissue only when activated. Indeed, the recruitment of the collagen fibers has been hypothesized as the underlying mechanism for the mechanical stiffening with increasing stress in arteries.
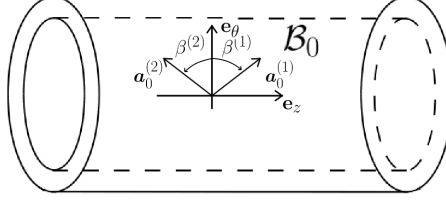
Figure 2: Directions $\boldsymbol{a}_0^{(i)}$, $i = 1, 2$, of the families of collagen fibers in the reference configuration $\mathcal{B}_0$.

When the collagen fibers are activated, the isochoric strain energy function $\overline{\mathcal{W}}$ characterizing transversely isotropic materials, that we indicate by $\overline{\mathcal{W}}_{ti}$, is decomposed into the sum of the load-bearing contributions provided by the background material and the collagenous constituent as:

$$\overline{\mathcal{W}}_{ti} = \overline{\mathcal{W}}_{ti}^{bg} + \overline{\mathcal{W}}_{ti}^{fibers}, \tag{14}$$

where $\overline{\mathcal{W}}_{ti}^{bg}$ characterizes the background material and $\overline{\mathcal{W}}_{ti}^{fibers}$ models the fiber-reinforcing component of the tissue. As described in [2], isotropic laws as those presented in Sec. 2.2.3 (SVK, EXP1, EXP2) can be used to describe the background material. Conversely, the component $\overline{\mathcal{W}}_{ti}^{fibers}$ of $\overline{\mathcal{W}}_{ti}$ takes into account for the transversely isotropic effects in the mechanical response of N families of collagen fibers. For any point $\boldsymbol{X}$ in the reference configuration $\mathcal{B}_0$, each family of collagen fibers is endowed with a characteristic direction $\boldsymbol{a}_0^{(i)}$, for $i = 1 \ldots N$, as highlighted in Fig. 2. Due to the weak interactions between the fiber families [2], the strain energy function $\overline{\mathcal{W}}_{ti}^{fibers}$ is written as the sum of N strain energy functions, $\overline{\mathcal{W}}_{ti}^{fibers,(i)}$, each of them characterizing the mechanical behavior of the i-th family, as:

$$\overline{\mathcal{W}}_{ti}^{fibers} = \sum_{i=1}^{N} \overline{\mathcal{W}}_{ti}^{fibers,(i)}. \tag{15}$$

The function $\overline{\mathcal{W}}_{ti}^{fibers,(i)}$, due to frame indifference requirements, can be formulated in terms of the so called modified pseudo-invariants of $\overline{\boldsymbol{C}}$ and the second order tensor $(\boldsymbol{a}_0^{(i)} \otimes \boldsymbol{a}_0^{(i)})$ associated to the i-th family [8, 51], indicated by $\overline{I}_4^{(i)}$ and $\overline{I}_5^{(i)}$, as:

$$\overline{\mathcal{W}}_{ti}^{fibers,(i)} = \overline{\mathcal{W}}_{ti}^{fibers,(i)}(\overline{I}_4^{(i)}, \overline{I}_5^{(i)}), \tag{16}$$

where

$$\overline{I}_4^{(i)} = \mathrm{Tr}\left(\overline{\boldsymbol{C}}(\boldsymbol{a}_0^{(i)} \otimes \boldsymbol{a}_0^{(i)})\right) = J^{-2/3}\,\mathrm{Tr}\left(\boldsymbol{C}(\boldsymbol{a}_0^{(i)} \otimes \boldsymbol{a}_0^{(i)})\right) = J^{-2/3}I_4^{(i)}, \tag{17}$$

and

$$\overline{I}_5^{(i)} = \mathrm{Tr}\left(\overline{\boldsymbol{C}}^2(\boldsymbol{a}_0^{(i)} \otimes \boldsymbol{a}_0^{(i)})\right) = J^{-4/3}\,\mathrm{Tr}\left(\boldsymbol{C}^2(\boldsymbol{a}_0^{(i)} \otimes \boldsymbol{a}_0^{(i)})\right) = J^{-4/3}I_5^{(i)}, \tag{18}$$

being $I_4^{(i)}$ and $I_5^{(i)}$ the fourth and fifth invariants associated to $\boldsymbol{C}$ and the tensor $(\boldsymbol{a}_0^{(i)} \otimes \boldsymbol{a}_0^{(i)})$. From the mechanical point of view, $I_4^{(i)}$ corresponds to the square of the stretch of the body along the fiber direction $\boldsymbol{a}_0^{(i)}$, or alternatively, it can be interpreted as the square of the length of the deformed fiber in the current configuration; $I_5^{(i)}$ measures the deformations of the i-th collagen fiber under shear conditions [52]. In the transversely isotropic models under consideration, we set either $\overline{\mathcal{W}}_{ti}^{bg} = \overline{\mathcal{W}}_{iso}^{EXP1}$ or $\overline{\mathcal{W}}_{ti}^{bg} = \overline{\mathcal{W}}_{iso}^{EXP2}$. The isochoric strain energy function for the single collagen fiber family $\overline{\mathcal{W}}_{ti}^{fibers,(i)}$ in Eq. (15) is chosen as a second order exponential law along the fiber direction, that is:

$$\overline{\mathcal{W}}_{ti}^{fibers,(i)}\left(\overline{I}_4^{(i)}, \overline{I}_5^{(i)}\right) = \overline{\mathcal{W}}_{ti}^{fibers,(i)}\left(\overline{I}_4^{(i)}\right) = \frac{\alpha^{(i)}}{2\gamma^{(i)}}\left(e^{\gamma^{(i)}(\overline{I}_4^{(i)} - \|\boldsymbol{a}_A^{(i)}\|^2)^2} - 1\right), \tag{19}$$

7

where $\alpha^{(i)}$ and $\gamma^{(i)}$ are the mechanical stiffness and level of nonlinearity characterizing the i-th family of collagen fibers, respectively, and $\|\boldsymbol{a}_A^{(i)}\|$ is called the activation length of the i-th family of collagen fibers. From the modeling point of view, $\|\boldsymbol{a}_A^{(i)}\|$ is the length at which the recruitment of the i-th family of collagen fibers occurs. The i-th family of collagen fibers is considered activated, i.e. it contributes to the mechanical response of the arterial tissue, when $\overline{I}_4^{(i)}$ is higher than the square of the activation length $\|\boldsymbol{a}_A^{(i)}\|$ [21, 44]. According to [20, 44], the activation length corresponds to the length of the collagen fibers in the reference configuration $\mathcal{B}_0$; therefore, for this class of models, the i-th family of collagen fibers is activated whenever the activation condition, $\overline{I}_4^{(i)} > \|\boldsymbol{a}_0^{(i)}\|^2$, is satisfied. In literature (see [19, 20, 44, 53]), the length of the i-th fiber family in the reference configuration $\mathcal{B}_0$ is usually set to 1. In the following, this constitutive model will be indicated as EXP2-RC. On the other hand, according to the multi-mechanism model [21, 22], the recruitment of the i-th family of collagen fibers occurs whenever $\overline{I}_4^{(i)} > \|\boldsymbol{a}^{(i)}{}_{MM}\|^2$, where $\|\boldsymbol{a}^{(i)}{}_{MM}\|$ is the activation length associated to the i-th family in a deformed configuration of the body $\mathcal{B}_{MM}^{(i)}$, called the activation configuration. In [39], the activation length satisfies the condition $\|\boldsymbol{a}^{(i)}{}_{MM}\| > 1$ since, in the reference configuration $\mathcal{B}_0$, the collagen fibers are assumed of unitary length. The strain energy function for the collagen fibers in the multi-mechanism model will be indicated as EXP2-MM. We remark that the strain energy function $\overline{\mathcal{W}}_{ti}^{fibers,(i)}$ in Eq. (19) satisfies the polyconvexity condition for all states of deformations [44].

The full isochoric strain energy function $\overline{\mathcal{W}}_{ti}$ in Eq. (14) for transversely isotropic material reads as follows:

$$\overline{\mathcal{W}}_{ti}(\overline{I}_1, \overline{I}_2, \overline{I}_3, \overline{\mathbf{I}}_4, \overline{\mathbf{I}}_5) = \overline{\mathcal{W}}_{ti}^{bg}(\overline{I}_1, \overline{I}_2) + \overline{\mathcal{W}}_{ti}^{fibers}(\overline{\mathbf{I}}_4, \overline{\mathbf{I}}_5), \tag{20}$$

where $\overline{\mathbf{I}}_4 = \{\overline{I}_4^{(i)}\}_{i=1}^N$ and $\overline{\mathbf{I}}_5 = \{\overline{I}_5^{(i)}\}_{i=1}^N$ are the set of pseudo-invariants of the different fiber families. We remark that, similarly to Eq. (8), the dependency of $\overline{\mathcal{W}}_{ti}$ on $\overline{I}_3$ has been dropped since $\overline{I}_3 \equiv 1$. When including the activation condition in Eq. (20), the general formulation of the isochoric strain energy function $\overline{\mathcal{W}}_{ti}$ reads:

$$\overline{\mathcal{W}}_{ti} = \begin{cases} \overline{\mathcal{W}}_{ti}^{bg}(\overline{I}_1, \overline{I}_2), & \text{if } \overline{\mathbf{I}}_4 \leq \|\boldsymbol{a}_A\|^2, \\[2mm] \overline{\mathcal{W}}_{ti}^{bg}(\overline{I}_1, \overline{I}_2) + \overline{\mathcal{W}}_{ti}^{fibers}(\overline{\mathbf{I}}_4, \overline{\mathbf{I}}_5), & \text{if } \overline{\mathbf{I}}_4 > \|\boldsymbol{a}_A\|^2, \end{cases} \tag{21}$$

where $\|\boldsymbol{a}_A\|^2$ indicated the set of activation lengths $\{\|\boldsymbol{a}_A^{(i)}\|^2\}_{i=1}^N$. In Eq. (21), when assuming the activation length equal to the one in the reference configuration, $\|\boldsymbol{a}_A^{(i)}\|^2 = \|\boldsymbol{a}_0^{(i)}\|^2 = 1$, otherwise, for the multi-mechanism model, we have $\|\boldsymbol{a}_A^{(i)}\|^2 = \|\boldsymbol{a}^{(i)}{}_{MM}\|^2$. In Eq. (21), the condition $\overline{\mathbf{I}}_4 > \|\boldsymbol{a}_A\|^2$ is verified if there exists at least a fiber family i, with $i = 1, \ldots, N$, such that $\overline{I}_4^{(i)} > \|\boldsymbol{a}_A^{(i)}\|^2$. It is worth pointing out that, when the collagen fibers contribute to the mechanical response of the tissue, the isochoric part of the first Piola-Kirchhoff tensor $\overline{\boldsymbol{P}}$ for transversely isotropic models in Eq. (6) reads as follows:

$$\overline{\boldsymbol{P}}_{ti} = \overline{\boldsymbol{P}}_{ti}^{bg} + \overline{\boldsymbol{P}}_{ti}^{fibers} = \overline{\boldsymbol{P}}_{ti}^{bg} + \sum_{i=1}^N \overline{\boldsymbol{P}}_{ti}^{fibers,(i)}. \tag{22}$$

We include the collagen recruitment in the definition of $\overline{\boldsymbol{P}}_{ti}$ by means of an activation function that multiplies the contribution $\overline{\boldsymbol{P}}_{ti}^{fibers,(i)}$ as follows:

$$\overline{\boldsymbol{P}}_{ti} = \overline{\boldsymbol{P}}_{ti}^{bg} + \sum_{i=1}^N \left(\frac{1}{\pi} \arctan(\epsilon(\overline{I}_4^{(i)} - \|\boldsymbol{a}_A^{(i)}\|^2)) + \frac{1}{2} \right) \overline{\boldsymbol{P}}_{ti}^{fibers,(i)}, \tag{23}$$

where ϵ is a dimensionless user-specified parameter which we choose as $\epsilon = 5.0 \cdot 10^5$ to model the abrupt recruitment of the collagen fibers.

2.3 Determination of the material parameters from experimental data

In order to characterize the mechanical behavior of the healthy arterial tissue, it is necessary to estimate the material parameters of the isochoric constitutive models described in Sec. 2.2.2. In this work, the

material parameters of each isochoric model are determined by computing the least-squares approximation [54] of experimental measurements of the strain-stress relation of cerebral arteries [15]. In [15] quasi-static inflation tests up to the transmural pressure (ΔP) of 200 mmHg on cylindrical specimens of healthy human anterior cerebral artery (ACA) are shown. In this work, similarly to [21, 22], the ACA is modeled as a cylindrical membrane of undeformed internal radius (r_0) and thickness (h) composed of a homogeneous and incompressible material. We remark that, in virtue of the incompressibility assumption (i.e. $J = 1$), the volumetric function $\mathcal{U}$ in Eq.(5) is identically null, while the modified invariants of $\overline{\boldsymbol{C}}$ coincide with the principal invariants of $\boldsymbol{C}$, being $\overline{\boldsymbol{C}} \equiv \boldsymbol{C}$ (see Eqs. (9), (17), and (18)). In [15] the deformation of the internal radius is measured by the circumferential stretch, indicated by λ_r, that is defined as $\lambda_r = r/r_0$, with r being the deformed radius at a certain level of transmural pressure ΔP. In order to fit the experimental data we consider nonlinear functions $\mathcal{T} = \mathcal{T}(\lambda_r)$ (detailed in Secs. 2.3.1 and 2.3.2) that relate the membrane tension $\mathcal{T}$ to the circumferential stretch λ_r as in [21, 22, 55, 56]. In addition, the membrane tension is related to the transmural pressure by means of the Young-Laplace equation, $\mathcal{T} = r \, \Delta P$ ([15]). For a given constitutive model for the cerebral arterial tissue, the nonlinear approximation of the experimental data is computed by means of the Levenberg-Marquardt least-squares method [57].

Once the material parameters of a constitutive model have been estimated, the quality of the least-squares approximation is evaluated by means of the R^2 value [58] defined as:

$$R^2 = 1 - \frac{\displaystyle\sum_{i=1}^{n_s} \left(\mathcal{T}_i - \mathcal{T}(\lambda_r^i) \right)^2}{\displaystyle\sum_{i=1}^{n_s} \left(\mathcal{T}_i - \overline{\mathcal{T}} \right)^2}, \tag{24}$$

where n_s is the number of strain-stress experimental measurements $(\lambda_r^i, \mathcal{T}_i)$, for $i = 1, \ldots, n_s$, $\overline{\mathcal{T}}$ is the mean measured membrane tension, and $\mathcal{T}(\lambda_r^i)$ is the membrane tension evaluated at the measured deformation λ_r^i. The closer to one is the R^2 value corresponding to a constitutive model, the better is the data fitting.

Secs. 2.3.1 and 2.3.2 present the functions $\mathcal{T}(\lambda_r)$ used to approximate the experimental measurements for the constitutive models of Sec. 2.2.2 together with the values of the selected material parameters and the corresponding R^2 values. We recall that, as discussed in Sec. 2.2.1, the penalization parameter κ in Eq. (7) is not involved in the parameter estimation procedure; we set $\kappa = 9.0 \cdot 10^6$ dyn/cm^2.

2.3.1 Determination of the material parameters for isotropic models

For isotropic models, under the incompressibility assumption (i.e. $J = 1$), Eq. (5) reduces to

$$\mathcal{W} = \overline{\mathcal{W}}_{iso}(\overline{I}_1, \overline{I}_2) = \mathcal{W}_{iso}(I_1, I_2). \tag{25}$$

According to [22], the strain-stress function $\mathcal{T} = \mathcal{T}(\lambda_r)$ for the data fitting is

$$\mathcal{T}(\lambda_r) = \frac{h}{\lambda_r} \left(\lambda_r^2 - \frac{1}{\lambda_r^2} \right) \left(2 \frac{\partial \mathcal{W}_{iso}}{\partial I_1} + 2 \frac{\partial \mathcal{W}_{iso}}{\partial I_2} \right) \tag{26}$$

for each of the constitutive models of Sec. 2.2.3 ($\mathcal{W}_{iso}^{SVK}$, $\mathcal{W}_{iso}^{EXP1}$, and $\mathcal{W}_{iso}^{EXP2}$). Fig. 3(a) shows the least-squares approximation of the experimental data of [15] by means of the function $\mathcal{T} = \mathcal{T}(\lambda_r)$ for each of the isotropic constitutive models with the material parameters of Tab. 1. As indicated by the R^2 value in Tab. 1, in the case of the SVK model the experimental data are not properly approximated on the full range of transmural pressures. Conversely, the data fitting improves when the EXP1 and EXP2 models are considered. In these cases, as shown in Fig. 3(a), for transmural pressures higher than 50 mmHg, small differences are observed between the two approximated strain-stress relations. On the other hand, see Fig. 3(b), for low transmural pressures, the second order exponential (EXP2) model provides the best approximation of the data with respect to the other two isotropic model.
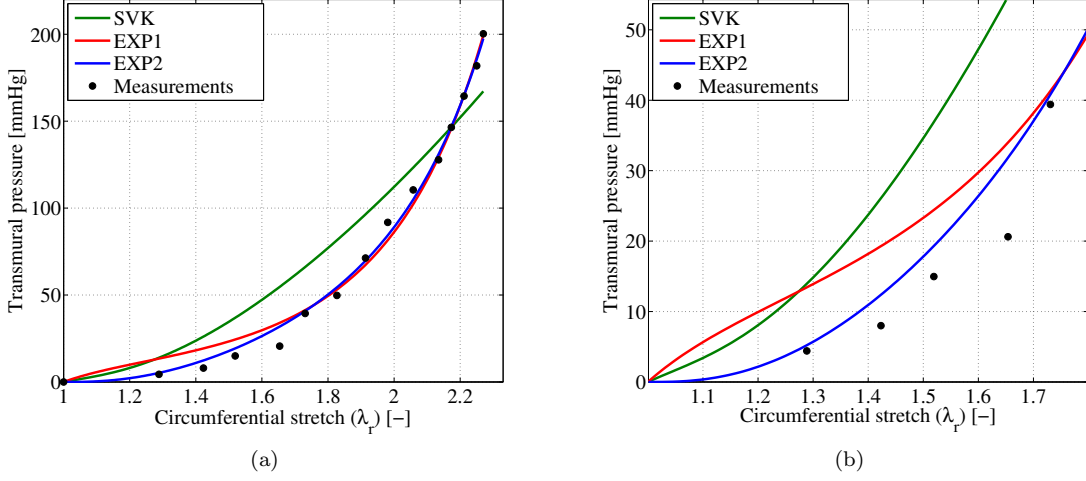
Figure 3: Least-squares approximation of the data in [15] using the isotropic models. Full range of transmural pressures $\Delta P \in [0, 200]$ mmHg (left); low transmural pressures regime $\Delta P \in [0, 40]$ mmHg (right).

Model ($\mathcal{W}_{iso}$)	Parameters	R^2
$\mathcal{W}_{iso}^{SVK}$	$E = 1.1420 \cdot 10^5, \nu = 0.4500$	0.9338
$\mathcal{W}_{iso}^{EXP1}$	$\alpha_1 = 7.6350 \cdot 10^4, \gamma_1 = 0.7410$	0.9942
$\mathcal{W}_{iso}^{EXP2}$	$\alpha_2 = 6.8220 \cdot 10^4, \gamma_2 = 0.0609$	0.9971

Table 1: Material parameters and R^2 values for the isotropic models. E, α_1, α_2 [dyn/cm^2]; ν, γ_1, γ_2 [-].

2.3.2 Determination of the material parameters for transversely isotropic models

Similarly to Eq. (25), under the incompressibility assumption (i.e. $J = 1$), Eq. (20) reduces to:

$$\mathcal{W} = \overline{\mathcal{W}}_{ti}(\overline{I}_1, \overline{I}_2, \overline{\mathbf{I}}_4, \overline{\mathbf{I}}_5) = \mathcal{W}_{ti}^{bg}(I_1, I_2) + \mathcal{W}_{ti}^{fibers}(\mathbf{I}_4, \mathbf{I}_5). \tag{27}$$

As in other works where transversely isotropic models describe the arterial tissue (e.g. [17, 21, 59]), we consider two families of collagen fibers oriented symmetrically with respect to the circumferential direction of the cylinder as in Fig. 2. In addition, we remark that, for transversely isotropic models, the material parameters $\alpha^{(i)}$ and $\gamma^{(i)}$ in Eq. (19) are the same for all families of fibers. According to [21], for the transversely isotropic models of Sec. 2.2.4 the function $\mathcal{T} = \mathcal{T}(\lambda_r)$ reads as :

$$\mathcal{T}(\lambda_r) = \frac{h}{\lambda_r}\left[2\left(\lambda_r^2 - \frac{1}{\lambda_r^2}\right)\frac{\partial\mathcal{W}_{ti}^{bg}}{\partial I_1} + \sum_{i=1}^{2} 2\frac{\partial\mathcal{W}_{ti}^{fibers,(i)}}{\partial I_4^{(i)}}\frac{\lambda_r^2\cos^2\beta^{(i)}}{\|\boldsymbol{a}_A^{(i)}\|^2}\right], \tag{28}$$

where $\beta^{(i)}$ is the angle between the characteristic direction of the i-th fiber family in the reference configuration $\mathcal{B}_0$, indicated by $\boldsymbol{a}_0^{(i)}$, and the circumferential axis $\mathbf{e}_\theta$ (see Fig. 2). We remark that in Eq. (28), due to the representation of the arterial tissue as a membrane, the recruitment of the collagen fibers will occur simultaneously throughout the thickness of the vessel wall [22]. In addition, we set $\beta^{(1)} = -\beta^{(2)}$ and $\|\boldsymbol{a}_A^{(1)}\|^2 = \|\boldsymbol{a}_A^{(2)}\|^2$. In order to include in the least-squares approximation the activation condition ($I_4^{(i)} >$

$\|\boldsymbol{a}_A^{(i)}\|^2$) of Eq. (21) we consider the following modified form of Eq. (28):

$$\mathcal{T}(\lambda_r) = \frac{h}{\lambda_r}\left[2\left(\lambda_r^2 - \frac{1}{\lambda_r^2}\right)\frac{\partial \mathcal{W}_{ti}^{bg}}{\partial I_1} + \sum_{i=1}^2 \left(\frac{1}{\pi}\arctan(\epsilon(I_4^{(i)} - \|\boldsymbol{a}_A^{(i)}\|^2)) + \frac{1}{2}\right)2\frac{\partial \mathcal{W}_{ti}^{fibers,(i)}}{\partial I_4^{(i)}}\frac{\lambda_r^2 \cos^2 \beta^{(i)}}{\|\boldsymbol{a}_A^{(i)}\|^2}\right], \quad (29)$$

to relate the membrane tension to the circumferential stretch. The activation stretch $\|\boldsymbol{a}_A^{(i)}\|^2$ depends on the angle $\beta^{(i)}$ and on the circumferential stretch ($\lambda_r^{A,(i)}$) at which the recruitment of the i-th family of collagen fibers occurs by means of the relation [21]:

$$\|\boldsymbol{a}_A^{(i)}\|^2 = (\lambda_r^{A,(i)})^2 \cos^2 \beta^{(i)} + \sin^2 \beta^{(i)}, \quad (30)$$

and we set $\lambda_r^{A,(1)} = \lambda_r^{A,(2)}$. As discussed in Sec. 2.2.4 we consider transversely isotropic models for which the collagen fibers are activated when their deformed length is either greater than their length in the reference configuration $\|\boldsymbol{a}_0^{(i)}\|$ or greater than a reference length $\|\boldsymbol{a}^{(i)}{}_{MM}\|$. In the first case (EXP2-RC model) such assumption implies that $\lambda_r^{A,(i)} = 1$ and theforore $\|\boldsymbol{a}_A^{(i)}\|^2 = \|\boldsymbol{a}_0^{(i)}\|^2 = 1$, for $i = 1, 2$. Conversely, for the multi-mechanism model (EXP2-MM model) $\lambda_r^{A,(i)} > 1$ and, therefore, $\|\boldsymbol{a}_A^{(i)}\|^2 > 1$, for $i = 1, 2$, [39]. In [21, 22] an estimation of the circumferential stretch of activation in Eq. (30) is provided based on the measurements reported in [15]. However, since no experimental observations on the circumferential stretch of activation were reported in [15], we consider $\lambda_r^{A,(1)}$ as an additional material parameter to be estimated for the EXP2-MM model.

As discussed in Sec. 2.2.4, we employ either the EXP1 or EXP2 model to describe the mechanical behavior of the background material. In the following, a transversely isotropic model will be indicated by the couple of strain energy functions used for the background material and the collagen fibers. Tab. 2 summarizes the material parameters and R^2 value for each of the transversely isotropic models under consideration. In Tab. 2, (α^{bg}, γ^{bg}) represent the material parameters characterizing the background material while ($\alpha^{(1)}, \gamma^{(1)}, \beta^{(1)}, \lambda_r^{A,(1)}$) are the material parameters for the single family of collagen fibers. We remark that the least-squares approximation of the data improves when transversely isotropic models are used with respect to isotropic models (Tab. 1). In addition, when the multi-mechanism model describes the collagen fibers the approximation of the experimental data is further improved with respect to the EXP2-RC model. Fig. 4(a) shows the membrane tension $\mathcal{T}(\lambda_r)$ for the (EXP1, EXP2-RC) and (EXP1, EXP2-MM) models. Fig. 4(b) shows the function $\mathcal{T}(\lambda_r)$ when either the EXP1 or the EXP2 models describe the background material and the collagen fibers are represented by the EXP2-MM model. In this case, the estimation of the circumferential stretch of activation $\lambda_r^{A,(1)}$ is strongly affected by the choice of the model for the background material (see Fig. 4(b) and Tab. 2). This is due to the fact that, as shown in Fig. 3(b), the EXP2 model fits better than the EXP1 law the data in the low pressure regime; therefore, when using the EXP2 model for the background material, the collagen fibers are activated at a higher activation circumferential stretch in order to fit the high transmural pressure regime.

We observe that, in Figs. 4(a) and 4(b), the recruitment of the collagen fibers at finite strains induces the sharp change in the membrane tension $\mathcal{T}(\lambda_r)$ around the circumferential stretch of activation $\lambda_r^{A,(1)}$. Although the (EXP2, EXP2-MM) model gives the best least-squares approximation of the experimental measurement, it will not be employed in the numerical simulations of healthy cerebral arterial tissue due to numerical issues related to the numerical solution of the structural mechanics problem (3) [60].

2.4 Mathematical modeling of elastin weakening

As described in Sec. 1, the onset of cerebral aneurysms is related to the mechanical degradation of the mechanical properties of the elastin in the media layer. We describe the weakening of the arterial tissue that occurs in diseased states of arteries (e.g. during the early phases of the formation of a cerebral aneurysm) by means of an isotropic damage model. Following the approach proposed in [38, 61], a dimensionless weakening parameter $D \in [0, 1)$ is used to represent the level of mechanical weakening affecting the material. The

Model ($\mathcal{W}_{ti}$)	Material Parameters	R^2
$\mathcal{W}_{ti}^{EXP1} + \mathcal{W}_{ti}^{EXP2\text{-}RC}$	$\alpha_{ti}^{bg} = 1.7471 \cdot 10^4$, $\gamma_{ti}^{bg} = 0.8620$ $\alpha^{(1)} = 1.4979 \cdot 10^5$, $\gamma^{(1)} = 0.5736$ $\beta^{(1)} = 0.9865$	0.9951
$\mathcal{W}_{ti}^{EXP2} + \mathcal{W}_{ti}^{EXP2\text{-}RC}$	$\alpha_{ti}^{bg} = 6.8220 \cdot 10^4$, $\gamma_{ti}^{bg} = 0.8620$ $\alpha^{(1)} = 6.008 \cdot 10^{-6}$, $\gamma^{(1)} = 0.8211$ $\beta^{(1)} = 1.4984$	0.9971
$\mathcal{W}_{ti}^{EXP1} + \mathcal{W}_{ti}^{EXP2\text{-}MM}$	$\alpha_{ti}^{bg} = 3.5270 \cdot 10^4$, $\gamma_{ti}^{bg} = 0.3424$ $\alpha^{(1)} = 1.3370 \cdot 10^5$, $\gamma^{(1)} = 0.2141$ $\beta^{(1)} = 0.7473$, $\lambda_r^{A,(1)} = 1.5009$	0.9980
$\mathcal{W}_{ti}^{EXP2} + \mathcal{W}_{ti}^{EXP2\text{-}MM}$	$\alpha_{ti}^{bg} = 5.5420 \cdot 10^4$, $\gamma_{ti}^{bg} = 3.0 \cdot 10^{-4}$ $\alpha^{(1)} = 1.3087 \cdot 10^5$, $\gamma^{(1)} = 0.5133$ $\beta^{(1)} = 0.8251$, $\lambda_r^{A,(1)} = 1.6538$	0.9985

Table 2: Parameters for the transversely isotropic models. α_{ti}^{bg}, $\alpha^{(1)}$ [dyn/cm^2]; $\beta^{(1)}$ [rad]; γ_{ti}^{bg},$\gamma^{(1)}$, $\lambda_r^{A,(1)}$ [-].
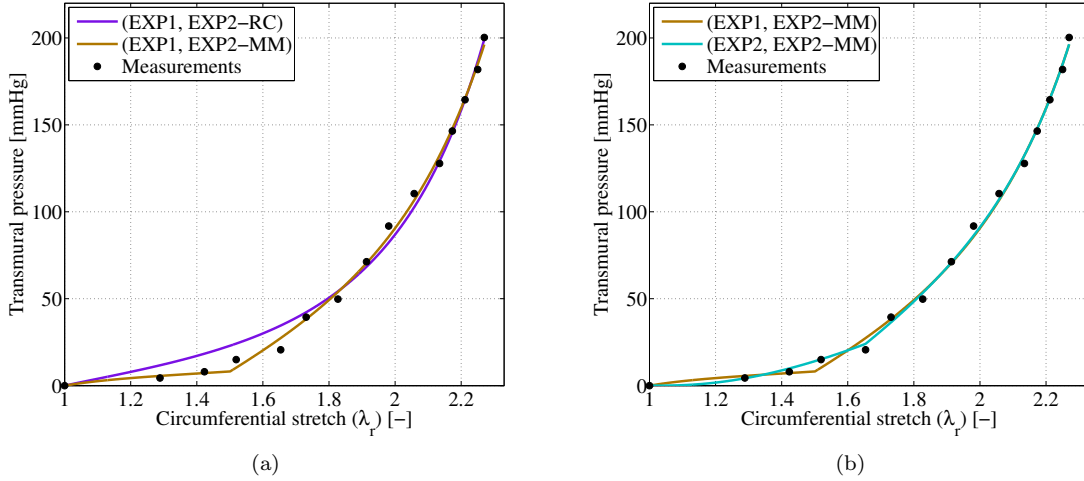
Figure 4: Least-squares approximation of the data in [15] using the transversely isotropic models.

unhealthy arterial tissue is then described by means of one of the constitutive models described in Sec. 2.2.2 for which the parameter representing the mechanical stiffness of the material is reduced by a factor of D. The arterial tissue is healthy and its mechanical properties intact when $D = 0$, while its full mechanical failure occurs when $D \to 1$.

As discussed in Sec. 2.1 the choice of the isochoric strain energy function $\overline{\mathcal{W}}$ (either isotropic or transversely isotropic) characterizes the mathematical description of the arterial tissue. When describing an unhealthy state of the arterial tissue, the weakening factor $(1 - D)$ affects only the isochoric part in the additive decomposition of the strain energy function (see Eq. (5)). Therefore, when using isotropic laws to model the unhealthy vessel wall, Eq. (5) is transformed as follows:

$$\mathcal{W}_{iso}(J, \overline{I}_1, \overline{I}_2; D) = \mathcal{U}(J) + \overline{\mathcal{W}}_{iso}(\overline{I}_1, \overline{I}_2; D). \tag{31}$$

When the vessel wall is described by the transversely isotropic model of Eq. (21), the weakening factor could affect the strain energy for the background material $\overline{\mathcal{W}}_{ti}^{bg}$ and the one describing the collagen fibers $\overline{\mathcal{W}}_{ti}^{fibers}$ in Eq. (14), or only one of the two. Based on the experimental observations on cerebral aneurysms, for which only the elastin is degraded in the early stages development of cerebral aneurysms, we assume that the weakening model affects only the mechanical contribution provided by the isotropic part $\overline{\mathcal{W}}_{ti}^{bg}$ of the strain energy function in Eq. (21). According to this choice, the transversely isotropic constitutive model for the unhealthy vessel wall reads:

$$\mathcal{W}_{ti}(J, \overline{I}_1, \overline{I}_2, \overline{\mathbf{I}}_4, \overline{\mathbf{I}}_5; D) = \mathcal{U}(J) + \overline{\mathcal{W}}_{ti}^{bg}(\overline{I}_1, \overline{I}_2; D) + \overline{\mathcal{W}}_{ti}^{fibers}(\overline{\mathbf{I}}_4, \overline{\mathbf{I}}_5). \tag{32}$$

In [21, 39, 44, 62] the weakening parameter D which is a function of kinematics quantities that depend on the history of the deformations that occur during the motion of the body, such as the maximum deformation or the maximum value of elastic energy [44, 39]. We are interested in analyzing the influence on kinematics quantities of interest for the modeling of unhealthy cerebral arterial tissue of isotropic and transversely isotropic constitutive models at different levels of mechanical weakening of the arterial tissue. For this reason, we fix a priori different values for D in the constitutive models of Eqs. (31) and (32). In order to have consistent comparisons among the different numerical simulations, it is necessary to calibrate the weakening parameter D for the different constitutive models; we detail this aspect in Sec. 2.5.

2.5 Calibration of the weakening parameter D for unhealthy cerebral arterial tissue.

Based on the results obtained from the least-squares approximation of the experimental data, we represent the unhealthy cerebral arterial tissue by introducing the weakening parameter D in three of the constitutive models discussed in Sec. 2.2.2: the isotropic EXP2 model, and the transversely isotropic models (EXP1, EXP2-RC) and (EXP1, EXP2-MM). The weakening parameter D is introduced in the constitutive models by means of the factor $(1 - D)$ multiplying the material parameters representing the mechanical stiffness of the material. Thus, the isochoric term $\overline{\mathcal{W}}_{iso}$ in Eq. (31) for the isotropic EXP2 model (indicated as U-EXP2) reads as:

$$\overline{\mathcal{W}}_{iso}(\overline{I}_1, \overline{I}_2; D) = \overline{\mathcal{W}}_{iso}^{U\text{-}EXP2}(\overline{I}_1, \overline{I}_2; D_{EXP2}) = \frac{(1 - D_{EXP2})\alpha_2}{2\gamma_2}\left(e^{\gamma_2(\overline{I}_1 - 3)^2} - 1\right). \tag{33}$$

The weakened background material in the transversely isotropic models is described by the following modified form of the EXP1 model (indicated as U-EXP1):

$$\overline{\mathcal{W}}_{ti}^{bg}(\overline{I}_1, \overline{I}_2; D) = \overline{\mathcal{W}}_{iso}^{U\text{-}EXP1}(\overline{I}_1, \overline{I}_2; D_{EXP1}) = \frac{(1 - D_{EXP1})\alpha^{bg}}{2\gamma^{bg}}\left(e^{\gamma^{bg}(\overline{I}_1 - 3)} - 1\right). \tag{34}$$

In the following, the transversely isotropic models for unhealthy cerebral arterial tissue will be indicated as (U-EXP1, EXP2-RC) and (U-EXP1, EXP2-MM), respectively, and $D_{EXP1}^{EXP2\text{-}RC}$ and $D_{EXP1}^{EXP2\text{-}MM}$ will represent the weakening paramter affecting the material properties of the background material in the (U-EXP1, EXP2-RC) and (U-EXP1, EXP2-MM), respectively. As pointed out in Sec. 2.4, the mechanical weakening of the tissue affects only the mechanical properties of the background material (Eq. (32)). Although different constitutive models can be adjusted to a set of experimental measurements in order to represent the healthy cerebral arterial tissue (Sec. 2.3), the choice of the weakening parameter D in Eqs. (33) and (34) has an important effect on the characterization of unhealthy cerebral arterial tissues. Fig. 5 shows the strain-stress functions $\mathcal{T}(\lambda_r)$ of Figs. 3(a) and 4(a) for the EXP2, (EXP1, EXP2-RC) and (EXP1, EXP2-MM) models for different values of the weakening parameter D. We observe that, for $D > 0.6$ the three curves do not interesect in the physiological range of transmural pressures ($\Delta P \in [70, 150]$). For this reason, the proper calibration of the weakening parameter D according to the model describing the vessel wall is necessary. We have calibrated the values of the parameter D for the three constitutive models with respect to a reference value for D_{ref} and the reference transmural pressure $\Delta P_{ref} = 110$ mmHg. More specifically, we have considered two cases.
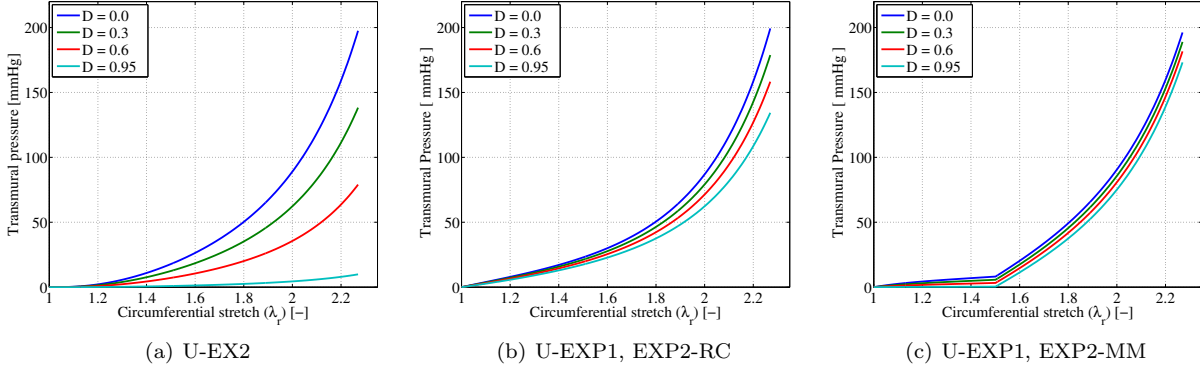
13

Figure 5: Functions $\mathcal{T}(\lambda_r)$ for different values of the weakening parameter D.

Firstly, we have fixed $D_{ref} = D_{EXP1}^{EXP2\text{-}MM} = 0.75$ for the (U-EXP1, EXP2-MM) model and determined the values of D_{EXP2} and $D_{EXP1}^{EXP2\text{-}RC}$ for the remaining two models such that the three functions $\mathcal{T} = \mathcal{T}(\lambda_r)$ intersect at the reference transmural pressure ΔP_{ref}. Then, we followed the same approach considering $D_{ref} = D_{EXP1}^{EXP2\text{-}RC} = 0.6$ for the (U-EXP1, EXP2-RC). We remark that in the latter case, as shown in Fig. 5(c), it is not possible to find a value of $D \in [0, 1)$ for which the (U-EXP1, EXP2-MM) model yield the reference deformation at the reference pressure. Fig. 6 shows the functions $\mathcal{T} = \mathcal{T}(\lambda_r)$ for the three constitutive models under consideration with the material parameters of Tabs. 1 and 2 and the values of the weakening parameter D summarized in Tab. 3.

Case	Weakening parameter D
Case 1	$D_{ref} = D_{EXP1}^{EXP2\text{-}MM} = 0.7500$, $D_{EXP1}^{EXP2\text{-}RC} = 0.3010$, $D_{EXP2} = 0.1103$
Case 2	$D_{ref} = D_{EXP1}^{EXP2\text{-}RC} = 0.6000$, $D_{EXP2} = 0.2641$

Table 3: Values for the weakening parameter D used in the numerical simulations.

3 Numerical approximation: the Finite Element Method

Problem (3) is solved by means of the Finite Element Method [63]. With this aim, let us introduce the Hilbert space V of functions $V(\mathcal{B}_0) = [H^1_{\Gamma_D}(\mathcal{B}_0)]^3 = \left\{ \boldsymbol{\psi} \in [H^1(\mathcal{B}_0)]^3 \text{ s.t. } \boldsymbol{\psi} = \mathbf{0} \quad \text{on } \Gamma_D \right\}$, for which the weak formulation of problem (3) reads :

find $\boldsymbol{d} = \boldsymbol{d}(\boldsymbol{X}) \in V$:

$$\int_{\mathcal{B}_0} \boldsymbol{P}(\boldsymbol{d}) : \nabla \boldsymbol{\psi} \, d\mathcal{B}_0 = \oint_{\Gamma_{in}} -p\boldsymbol{n} \cdot \boldsymbol{\psi} \, d\Gamma_{in} \qquad \forall \boldsymbol{\psi} \in V. \tag{35}$$

The discrete problem is obtained by approximating the reference configuration $\mathcal{B}_0$ by $\mathcal{B}_0^h$, a conforming mesh (triangulation) of $\mathcal{B}_0$, and by considering a finite dimensional subspace $V_h = (X_h^p \cap V) \subset V$ composed of Lagrangian, piecewise continuous polynomial basis functions of local polynomial degree $p \geq 1$ defining the space (X_h^p). Let $\{\boldsymbol{\psi}_A\}_{A=1}^{N_h}$, where $N_h := \dim(V_h)$, be the Lagrangian basis of V_h, in the form $\boldsymbol{\psi}_A = (\phi_A \mathbf{e}_1 + \phi_A \mathbf{e}_2 + \phi_A \mathbf{e}_3)$, where ϕ_A is a scalar Lagrangian function of V_h defined on the mesh $\mathcal{B}_0^h$, and $(\mathbf{e}_1, \mathbf{e}_2, \mathbf{e}_3)$ is the Euclidean base in $\mathbb{R}^3$. The discrete weak formulation of problem (3) is given by:
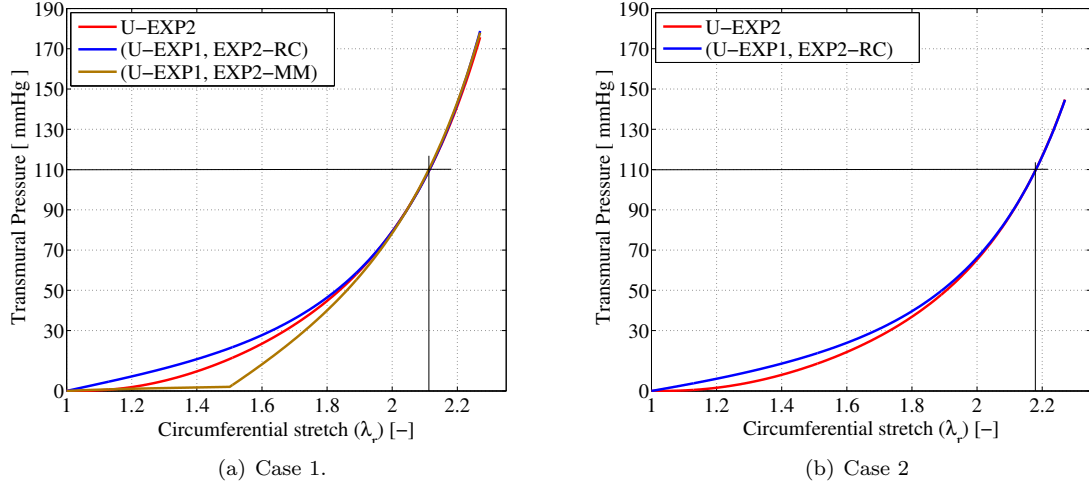
14

(a) Case 1. (b) Case 2

Figure 6: Functions $\mathcal{T}(\lambda_r)$ with the weakening parameters of Tab. 3.
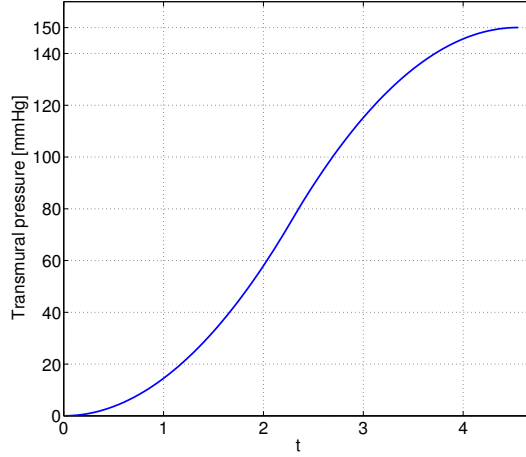
Figure 7: Inflating pseudo-time pressure profile $p(t)$ for problem (3).

find $\boldsymbol{d}_h = \boldsymbol{d}_h(\boldsymbol{X}) = \sum_{A=1}^{N_h} \sum_{j=1}^{3} (d_{h,j})_A \phi_A(\boldsymbol{X}) \mathbf{e}_j \in V_h :$

$$\int_{\mathcal{B}_0^h} \boldsymbol{P}(\boldsymbol{d}_h) : \nabla \boldsymbol{\psi}_A \ d\mathcal{B}_0^h = \oint_{\Gamma_{in}^h} -p_h \boldsymbol{n} \cdot \boldsymbol{\psi}_A \ d\Gamma_{in}^h \qquad \forall \boldsymbol{\psi}_A \in V_h, \tag{36}$$

where the j-th component of the displacement field is defined as $d_{h,j} = \sum_{A=1}^{N_h} (\boldsymbol{d}_{h,j})_A \phi_A$, with $j = 1, 2, 3$. In Eq. (36), Γ_{in}^h is the approximation of the internal surface Γ_{in} provived by the mesh $\mathcal{B}_0^h$, and p_h is a suitable approximation of the boundary data p on Γ_{in} (e.g. the L^2-projection of p onto $X_h^p(\Gamma_{in})$). We remark that the nonlinear constitutive relations considered in this work lead to the nonlinear problem (36) which is solved by means of the Newton method [54]. In order to guarantee the convergence of the Newton method for the

15

values of transmural pressures of interest, we use a pseudo-time approach, for which the inflating pressure is gradually applied by using a pseudo-time function $p(t)$, represented in Fig. 7. At each iteration of the Newton method, Eq. (36) is linearized with respect to the displacement field $\boldsymbol{d}$ (see [8, 44]) for which the tangent matrix $\left(J_{\boldsymbol{P}} = \dfrac{d\boldsymbol{P}(\boldsymbol{d})}{d\boldsymbol{d}} \right)$ of the first Piola-Kirchhoff tensor $\boldsymbol{P}(\boldsymbol{d})$ is evaluated, and the resulting linear system is solved by means of the GMRES method [64] preconditioned with the Additive-Schwarz method [65].

4   Numerical validation

We numerically validate the constitutive models described in Sec. 2.2.2, for which the material parameters are reported in Tabs. 1 and 2. Firstly, we show results of numerical simulations of static inflation tests on healthy cerebral arterial tissue. Then the weakening model discussed in Sec. 2.4 is considered and numerical simulations on unhealthy cerebral arterial tissue are discussed.

The computational domain representing the cerebral artery (see Fig. 1) is discretized by a tetrahedral mesh composed of 384,000 elements with $\mathbb{P}1$ Lagrangian finite elements for which the total number of degrees of freedom (DOFs) when approximating Eq. (36) is 241,200. The constitutive material models have been implemented in the finite element library LifeV [66] by means of an expression template assembly framework [67]. The numerical simulations have been run in parallel on 128 processors on the Cray XE6 supercomputer *Monte Rosa* at the Swiss national supercomputing center CSCS in Lugano, Switzerland.

4.1   Inflation tests on healthy cerebral tissue

We report in Fig. 8 the magnitude of the displacement field at the cross section located at $z = 1$ cm for $\Delta P = 150$ mmHg for the constitutive models of Sec. 2.2.2. As expected, the contour lines of the displacement are concentric with the largest displacement occurring at the inner surface of the artery. The displacement magnitude in Figs. 8(a)-(e) has been rescaled in order to show the correct qualitative behavior of all the numerical solutions; Fig. 8(f) presents the radial displacement through the thickness of the vessel wall for all the constitutive models. Figs. 9 and 10 show the strain-stress relations resulting from the least-squares approximation of the experimental measurements (see Sec. 2.3) and the ones obtained by the numerical simulations for the isotropic and transversely isotropic models, respectively. We report the circumferential stretch λ_r at the internal radius of the domain in order to compare it with the experimental measurement presented in [15]. The circumferential stretch was obtained from the numerical results computing the magnitude of the displacement field on Γ_{in} at the cross section $z = 1$ cm such that the effects of Dirichlet boundary conditions applied on Γ_D (see Fig. 1(a)) are negligible.

For the SVK isotropic model, as observed in Fig. 9(a), with pressures $\Delta P \in [70, 150]$ the strain-stress relation obtained from the numerical simulations does not adequately reproduce the one predicted by the data fitting, especially for the high values of ΔP. Conversely, a good agreement between the numerical and least-squares fitted strain-stress relations is observed for the EXP1 and EXP2 models. Such difference among the isotropic models can be ascribed to the choice of the penalization parameter κ in Eq. (7). The larger is κ, the smaller is the body displacement under the action of external forces. Thus, a value for κ that represents a good compromise between the need to model the quasi-incompressible behavior of arteries and to obtain a meaningful displacement field for a certain constitutive model, e.g. the EXP1 and EXP2 models, may become inappropriate for another one, e.g. the SVK model. However, in this study, in order to have a consistent comparison of the numerical results among the different cases under consideration, the same value for the penalty parameter has been used in our numerical simulations.

Fig. 10 shows the strain-stress curves obtained from the least-squares approximation and numerical simulation for the (EXP1, EXP2-RC) and (EXP1, EXP2-MM) models respectively. We observe a good agreement between the simulated strain-stress relations and the corresponding functions $\mathcal{T}(\lambda_r)$. For the (EXP1, EXP2-RC) model the highest error occurs for high transmural pressures while for the multi-mechanism model, i.e. (EXP1, EXP2-MM), the two curves are overlapped. However, in the latter case, the highest error occurs around the activation circumferential stretch. As discussed in Sec. 2.3.2, this is due to the fact that, in the
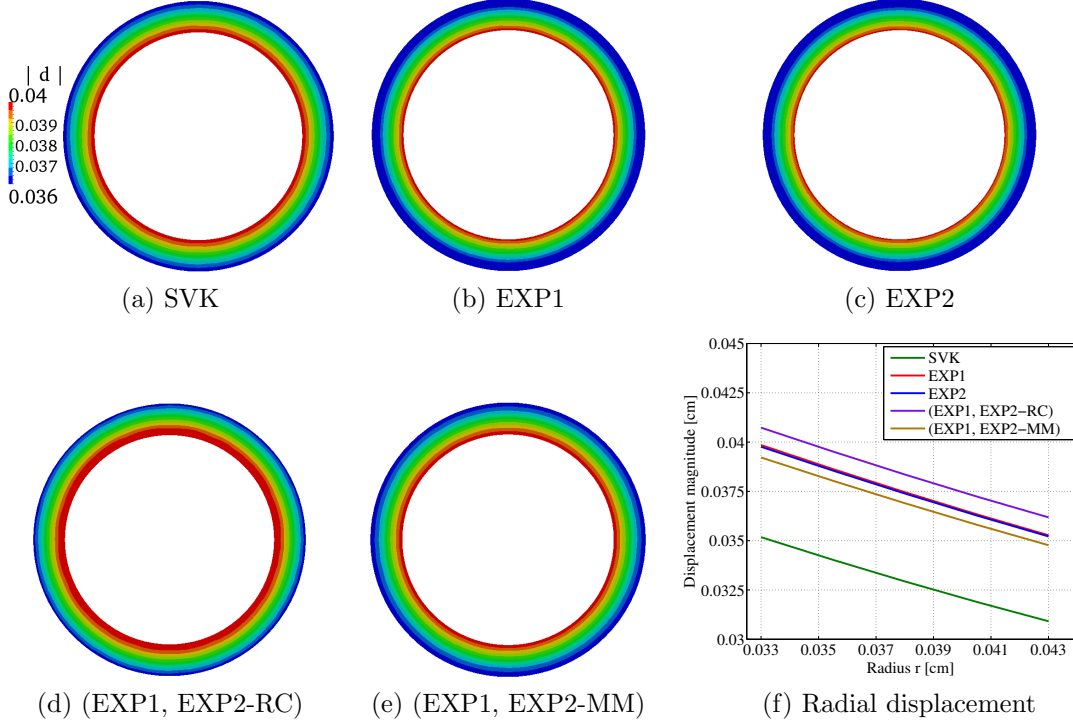
Figure 8: Displacement magnitude [cm] at the cross section at $z = 1$ cm and $\Delta P = 150$ mmHg for different material models.
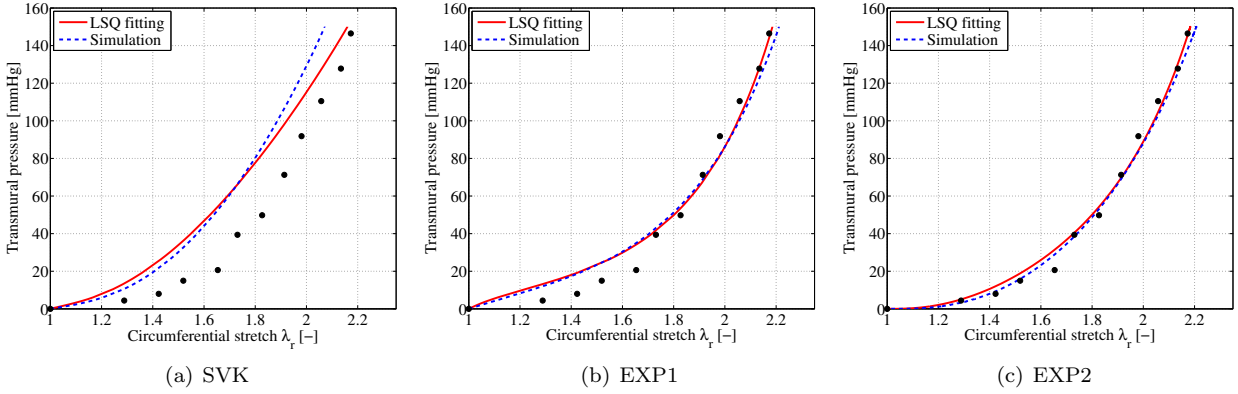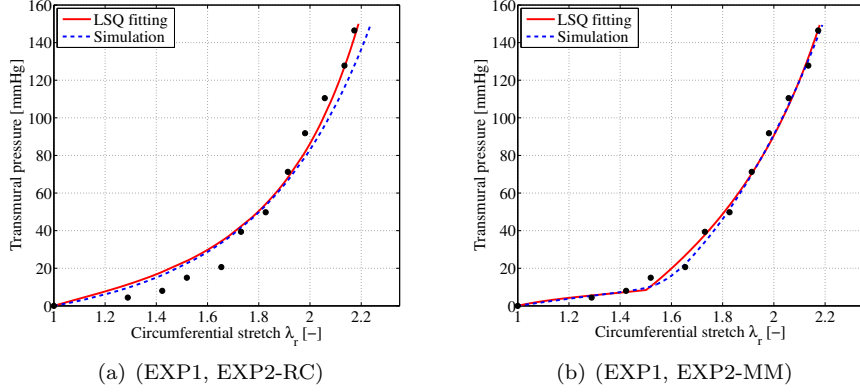

Figure 9: Strain-stress relation $\mathcal{T}(\lambda_r)$ and corresponding relation obtained from the numerical simulations for the isotropic models of Sec. 2.2.2. The dots represent the experimental data in [15].

data fitting, due to the membrane modeling of the vessel wall, the recruitment of the collagen fibers occurs simultaneously throughout the thickness of the vessel wall; this assumption does not hold in the numerical simulations since the arterial wall is described as a full three dimensional model.

Fig. 11 shows the relative error between the function $\mathcal{T}(\lambda_r)$ and the ones obtained from the numerical simulations. In the range of physiological transmural pressures, the maximum relative error is around 4% and it is observed for the isotropic SVK model. However, from the strain-stress measurements presented in [15], we can conclude that the relative error between the function $\mathcal{T}(\lambda_r)$ and the numerically simulated strain-

17

(a) (EXP1, EXP2-RC)　　　　　　　　(b) (EXP1, EXP2-MM)

Figure 10: Strain-stress relation $\mathcal{T}(\lambda_r)$ and corresponding relation obtained from the numerical simulations for the transversely isotropic models of Sec. 2.2.2. The dots represent the experimental data in [15].

(a) Isotropic models　　　　　　　　(b) Transversely isotropic models
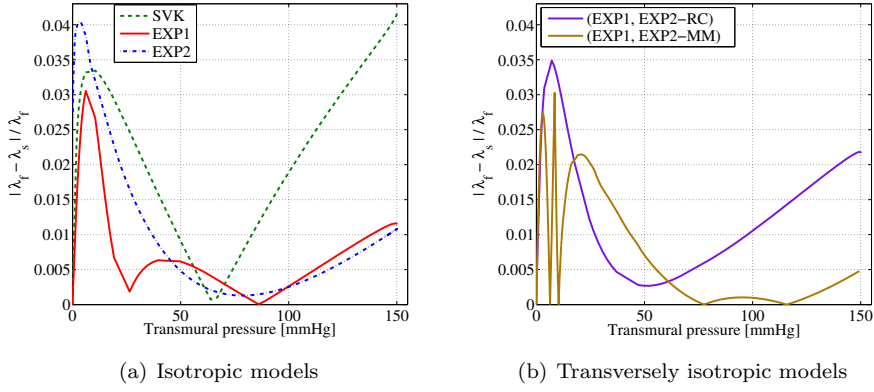
Figure 11: Relative error between the two strain-stress relations of Figs. 9 and 10 as a function of ΔP.

stress relations is compatible with (that is within the same range as) the one affecting the experimental measurements in [15]. In the physiological range of pressures for the EXP1, EXP2 and the transversely isotropic models, the relative error is below 2.5% confirming the good approximation of the least-squares fitted strain-stress relation by the numerical simulations. In the low pressures regime (i.e. for $\Delta P \in [0, 20]$ mmHg) the high relative errors are due to the use of linear finite elements for the discretization of Eq. (35) and they are observed for all the constitutive models. Indeed, from the numerical point of view, high values of the penalty parameter κ can lead to incorrect displacement fields or to locking phenomena when discretizing Eq. (35) by means of $\mathbb{P}1$ finite elements [53, 68]. In this work, the value for κ has been set in order to simulate the nearly-incompressible behavior of blood vessels for $\Delta P \in [70, 150]$ mmHg; this may lead to displacements which are not circumferentially symmetric for low transmural pressures, as shown in Fig. 12 (left). However, such asymmetry can be addressed, for instance, by discretizing Eq. (35) by means of quadratic ($\mathbb{P}2$) finite elements, as shown in Fig. 12 (right). For this comparison we employ the isotropic EXP1 model and, in order to have the same number of DOFs with the quadratic elements as in the linear case, a new mesh with 49,896 elements and 234,360 DOFs has been considered. In Fig. 12 we observe that for $\Delta P \in [70, 150]$ mmHg, the use of $\mathbb{P}2$ elements does not affect the circumferential stretch; therefore, we can conclude that the results presented in Figs. 9 and 10 are not significantly affected by the choice of the finite element space.

In order to highlight the influence of the bulk modulus on the approximation of the circumferential stretch,
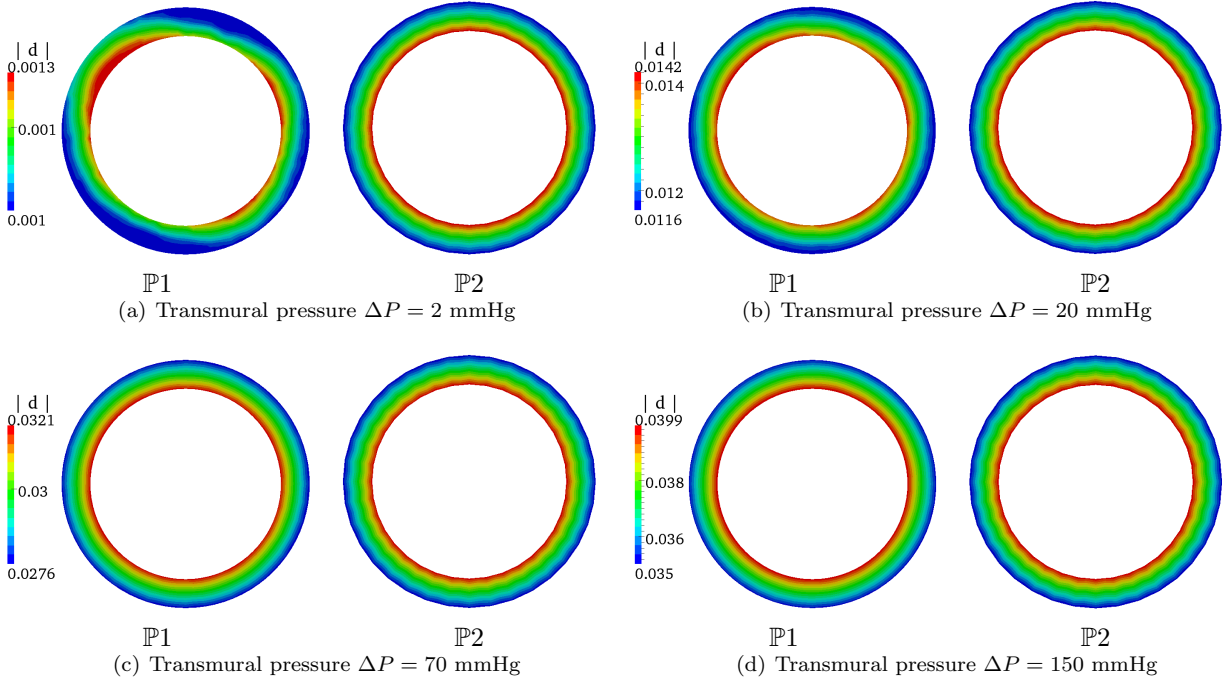
(a) Transmural pressure $\Delta P = 2$ mmHg

(b) Transmural pressure $\Delta P = 20$ mmHg

(c) Transmural pressure $\Delta P = 70$ mmHg

(d) Transmural pressure $\Delta P = 150$ mmHg

Figure 12: Displacement magnitude [cm] at different inflating pressures using the isotropic EXP1 model: using $\mathbb{P}1$ elements (#DOFs: 241,200)(left); using $\mathbb{P}2$ elements (#DOFs: 234,360)(right).
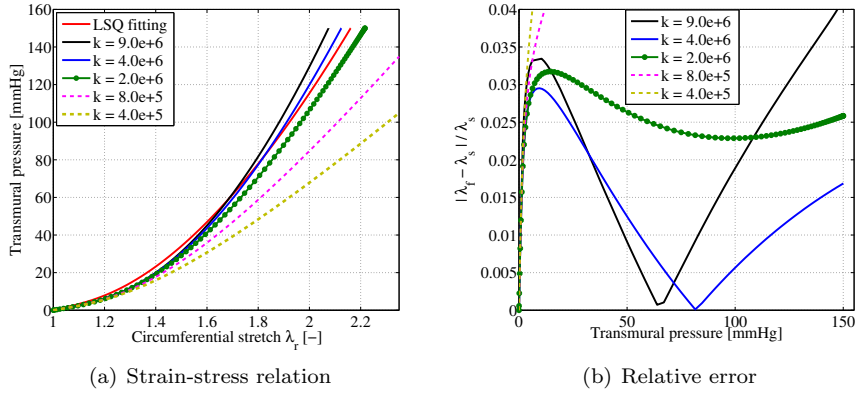

(a) Strain-stress relation

(b) Relative error

Figure 13: Strain-stress relations for different values of κ for the isotropic SVK model with the material parameters of Tab. 1.

Fig. 13(a) shows the strain-stress relations obtained for different values of κ in Eq. (7) using the SVK model with the material parameters reported in Tab. 1. We observe the influence of the penalization parameter on the computed displacement field and we show that, in this case, a different value of κ (i.e. $\kappa = 4.0 \cdot 10^6$ dyn/cm^2) would have led to a better approximation of the function $\mathcal{T} = \mathcal{T}(\lambda_r)$ in the range of transmural pressures of interest (see Fig. 13(b)).

Fig. 14 shows the approximation of the incompressibility constraint at the cross section $z = 1$ cm at the inflating pressure of 150 mmHg for the constitutive models of Sec. 2.2.2. The largest error on the
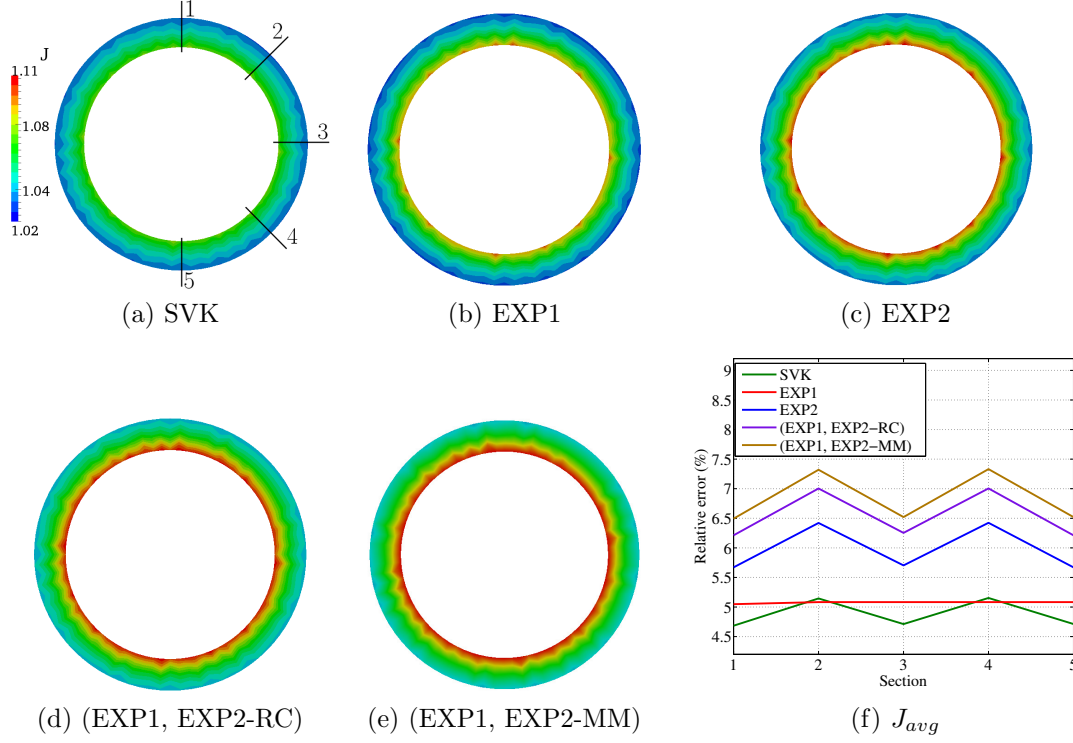
19

Figure 14: Volume ratio J and J_{avg} at $z = 1$ cm, $\Delta P = 150$ mmHg for the different material models; $\kappa = 9.0 \cdot 10^6$ dyn/cm^2.

approximation of the volumetric constraint ($J = 1$) occurs at the internal surface of the artery where the displacement is higher. The smallest error, around 4.5%, is obtained for the SVK model due to the smaller radial displacement (see Fig. 9(a)) of the vessel with respect to those obtained with the other constitutive laws. As discussed for Fig. 13, the choice of the penalization parameter κ strongly affects the numerical results for the SVK model. Fig. 15 shows the Jacobian J at the cross section $z = 1$ cm at the inflating pressure of 150 mmHg for two different values of κ ($\kappa = 4.0 \cdot 10^6$ and $\kappa = 9.0 \cdot 10^6$ dyn/cm^2) using the SVK model. We remark that, in Fig. 15, the Jacobian J is presented only for the values of κ such that the error on the incompressibility constraint is lower than 20%. For the SVK model, Fig. 13(a) shows that for $\Delta P \in [70, 150]$ mmHg, $\kappa = 4.0 \cdot 10^6$ dyn/cm^2 leads to a better approximation of the strain-stress relation $\mathcal{T}(\lambda_r)$ by means of the numerical simulations; however, such choice for the penalization parameter yields a poor approximation of the incompressibility constraint. For the constituive models of Sec. 2.2.2 the biggest error is reported for the transversely isotropic models, as in Fig. 14. This suggests that, once again, the value of the penalty parameter κ used for the numerical simulations should be tuned according to the constitutive law used to describe the tissue. Fig. 14-(f) shows the relative error (percentage) on the incompressibility constraint for $\Delta P = 150$ mmHg. More specifically, in Fig. 14-(f) the relative error is defined as $Er = 100(J_{avg} - 1)$, where J_{avg} is the average of the volume ratio along each one of the directions depicted in Fig. 14-(a). The oscillations reported in Fig. 14-(f) highlight the mesh dependence of the numerical results. The averaged Jacobians J_{avg} in Fig. 14-(f) indicate that the value of κ used in the numerical simulations leads to an acceptable approximation of the incompressibility constraint with the maximum relative error being approximatively 7%. In order to evaluate the mesh dependency on the approximation of the incompressibility constraint, numerical simulations of static inflation tests have been carried out for two additional meshes: one coarser and one finer than the reference mesh. For this numerical comparison, the tests have been carried out using the isotropic EXP1 model and $\mathbb{P}1$ finite elements. The coarser mesh is composed of 108,000 elements while the finer one is composed of 2,960,640 tetrahedra, yielding to 72,480 and 1,852,800 DOFs, respectively. Fig. 16
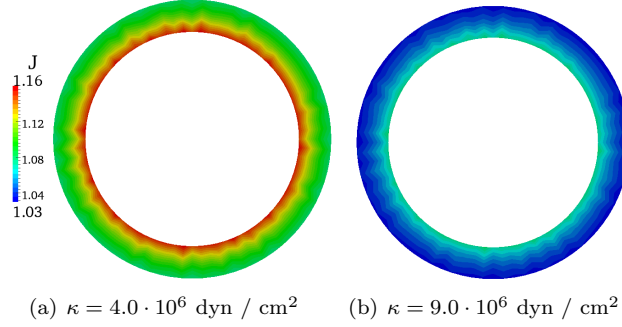
20

(a) $\kappa = 4.0 \cdot 10^6$ dyn / cm^2 (b) $\kappa = 9.0 \cdot 10^6$ dyn / cm^2

Figure 15: Volume ratio J for different values of the penalization parameter κ for the SVK model at the pressure $\Delta P = 150$ mmHg.
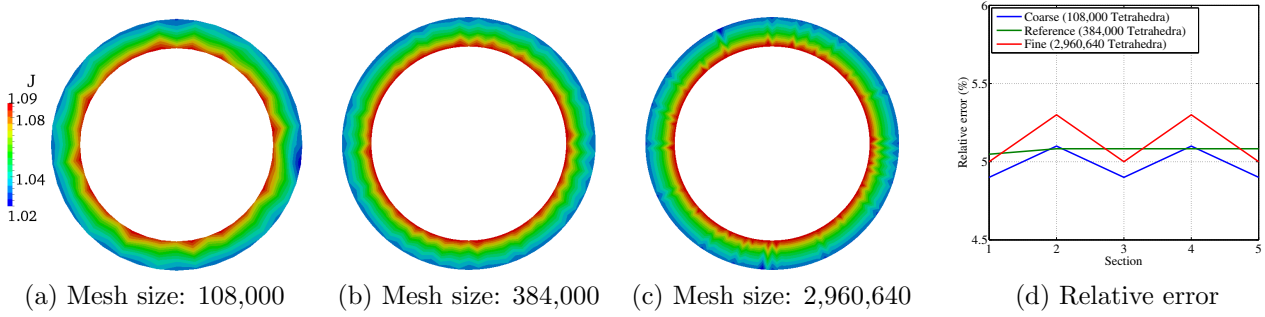

(a) Mesh size: 108,000   (b) Mesh size: 384,000   (c) Mesh size: 2,960,640   (d) Relative error

Figure 16: Volume ratio J for different meshes of the computational domain.

shows the approximation of the incompressibility constraint at the cross section $z = 1$ cm at the inflating pressure of 150 mmHg. No strong mesh refining effects are noticeable on the numerical solution suggesting that the approximation of the condition $J = 1$ is mainly affected by the choice of the penalty parameter κ.

The numerical validation of the isotropic and transversely isotropic constitutive models for the mechanical characterization of healthy cerebral arterial tissue has highlighted both modeling and numerical aspects that should be considered when simulating the arterial wall mechanics. From the modeling point of view, the least squares approximation and the numerical results suggest that, according to the range of transmural pressures of interest, a suitably calibrated isotropic model (as e.g. EXP1 or EXP2) can lead, in terms of the data fitting quality, to equivalent results than an anisotropic one, i.e. the (EXP1, EXP2-RC) model. In addition, the possibility of modeling the recruitment of the collagen fibers at finite strains (EXP1, EXP2-MM) instead of at zero strains leads to either a better approximation of the experimental measurements with a good agreement of the numerical results. Moreover, the numerical results obtained using the EXP1, EXP2, (EXP1, EXP2-RC) and (EXP1, EXP2-MM) indicate that when experimental observations of the characteristic directions of collagen fibers are not available on human specimen of arteries, an isotropic model can be a viable alternative to a transversely isotropic model; this has the advantage of reducing the number of material parameters that need to be estimated and the computational cost of the assembling of the tangent matrix of the first Piola-Kirchhoff tensor.

4.2 Inflation tests on unhealthy cerebral tissue

We now address the numerical simulation of unhealthy cerebral arteries by using the isotropic U-EXP2 and the transversely isotropic (U-EXP1, EXP2-RC) and (U-EXP1, EXP2-MM) laws. Among the isotropic models, the choice of U-EXP2 is motivated by the good data fitting and agreement between the curve $\mathcal{T}(\lambda_r)$
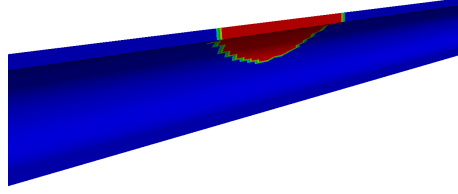
21

Figure 17: Representation of the weakened portion of the computational domain.

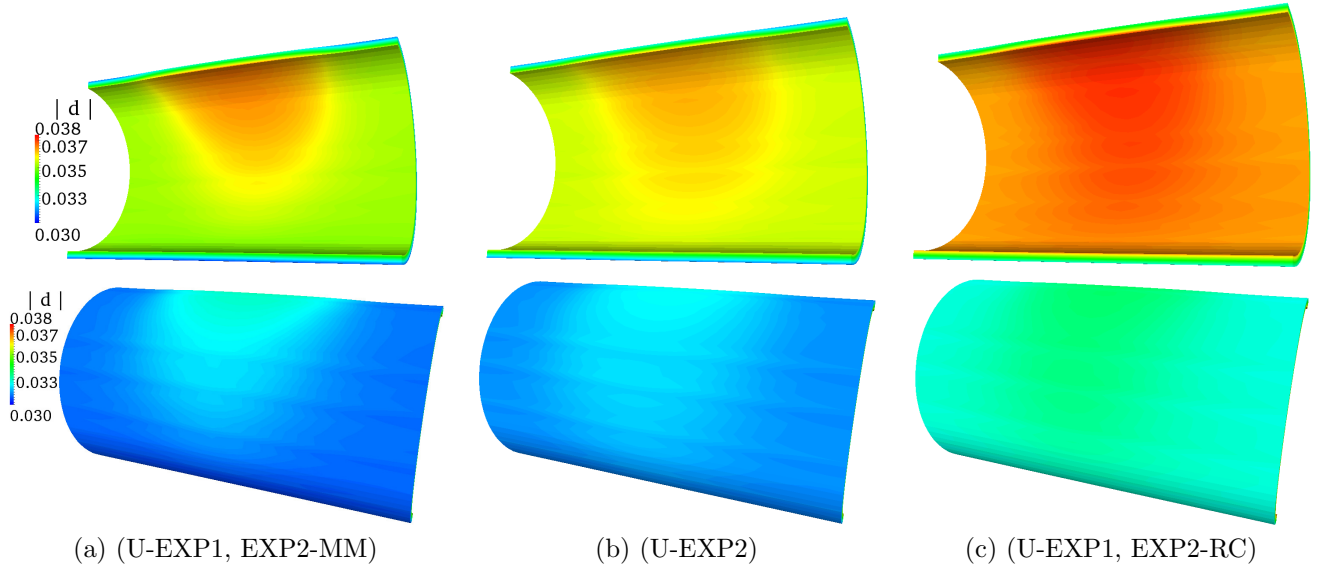(a) (U-EXP1, EXP2-MM)   (b) (U-EXP2)   (c) (U-EXP1, EXP2-RC)

Figure 18: Case 1: displacement field [cm] at the internal and external surfaces of the computational domain at $\Delta P_{ref} = 110$ mmHg.

and the numerical results showed in Fig. 9(c).

We assumed that the weakening of the material properties occurs in a limited portion of the domain, also referred as weakened region, that has been obtained from the intersection of the computational domain with a sphere of radius $r_s = 0.095$ cm and center $C = (0, 0.09, 1.0)$, as indicated in Fig. 17.

Figs. 18 and 19 show the displacement field on the deformed mesh for $\Delta P_{ref} = 110$ mmHg for Case 1 and Case 2 (Sec. 2.5). In Figs. 18 and 19 the mesh has been deformed according to the displacement field at the reference transmural pressure. We first notice that, for each of the two cases under consideration, the maximum value of the displacement magnitude is similar for all the constitutive models. This proves the correct calibration of the weakening parameter D both for Case 1 and Case 2. We also observe that, in both cases the pattern of the displacement fields is affected by the choice of the arterial wall model. The extension and shape of the area where the displacement field is influenced by the weakened region varies with the constitutive model and the weakening parameter D. We observe that in Case 2, where the weakening parameter D for the U-EXP2 and (U-EXP1, EXP2-RC) models is higher than in Case 1, the extension of the area where the displacement field is influenced by the weakened region becomes larger than in Case 1. In particular, for the (U-EXP1, EXP2-RC) model, it reaches the lower part of the cylinder and the displacement field is higher that the one reported for the U-EXP2 model. The displacement field reported in Figs. 18 and 19 indicate the formation of a bulge corresponding to the weakened region of the domain.

Figs. 20 and 21 report the volume ratio J at $z = 1$ at the reference transmural pressure for Case 1 and 2.
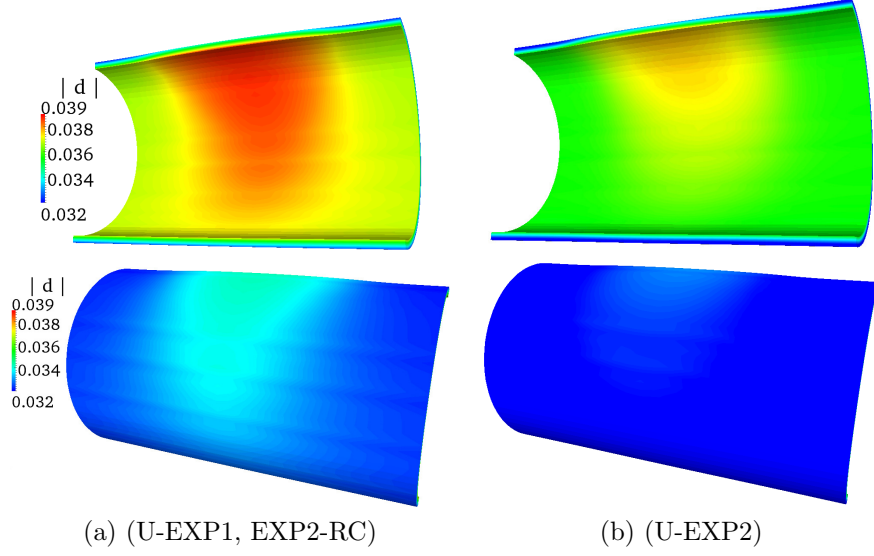
(a) (U-EXP1, EXP2-RC)   (b) (U-EXP2)

Figure 19: Case 2: displacement field [cm] at the internal and external surfaces of the computational domain at $\Delta P_{ref} = 110$ mmHg.
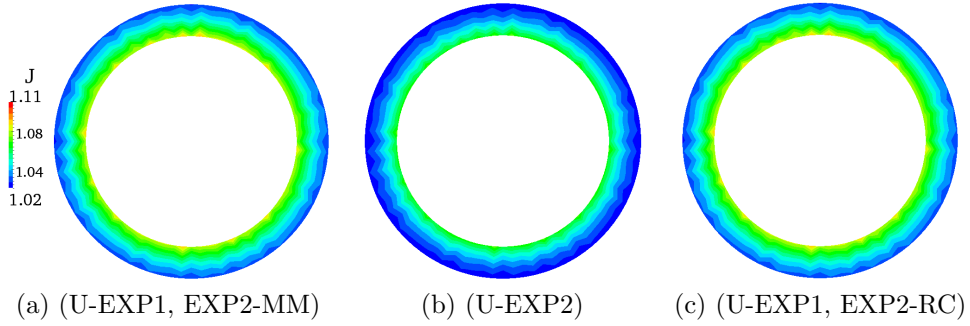

(a) (U-EXP1, EXP2-MM)   (b) (U-EXP2)   (c) (U-EXP1, EXP2-RC)

Figure 20: Case 1: Volume ratio J at $\Delta P = 110$ mmHg.

(a) (U-EXP1, EXP2-RC)   (b) (U-EXP2)
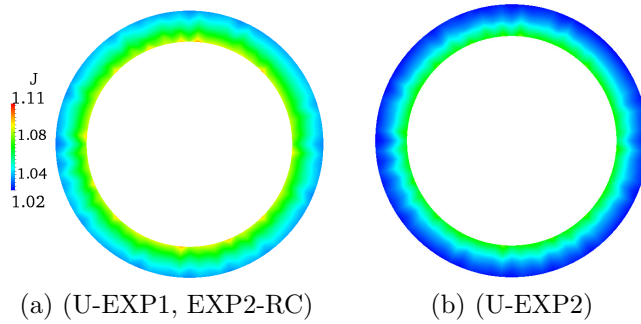
Figure 21: Case 2: Volume ratio J at $\Delta P = 110$ mmHg.

As already reported in Fig. 14, the approach used in this work to describe the nearly-incompressible behavior of arteries leads to an acceptable approximation of the incompressibility constraint.

Figs. 22, 23, 24 and 25 show the spatial distribution of the Von Mises stress σ_{VM}[8] in a central portion of the computational domain for Case 1 and Case 2. In both cases the σ_{VM} varies between $2.5 \cdot 10^5$ and
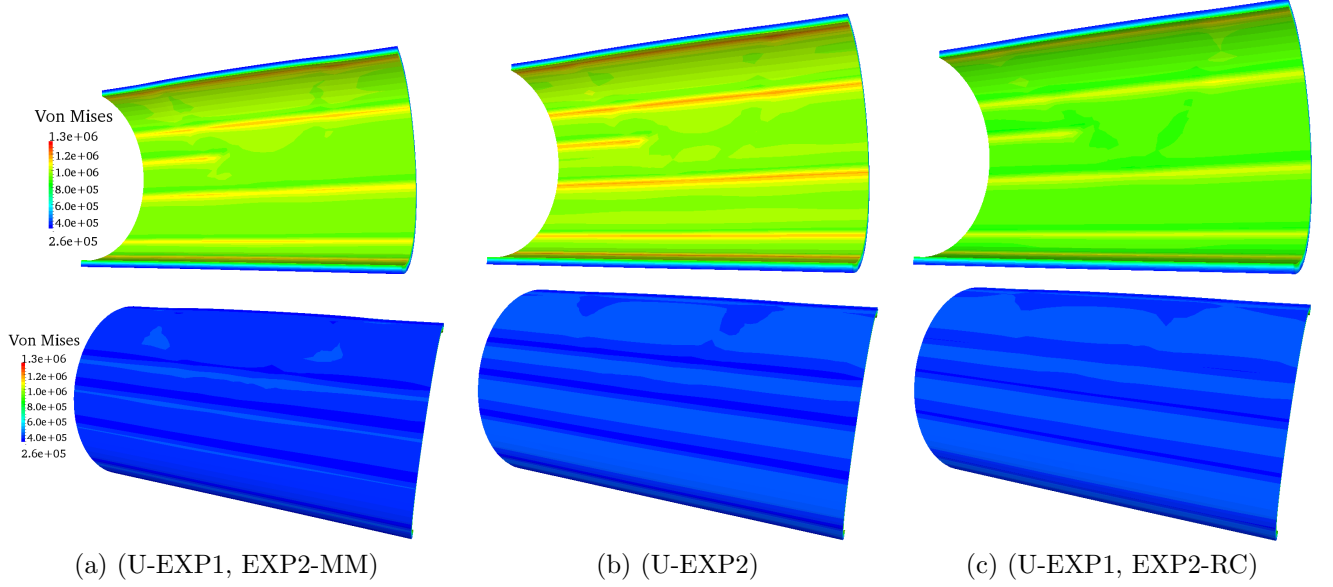
23

Figure 22: Case 1: Von Mises stress field $[\mathrm{dyn/cm^2}]$ at the internal and external surfaces of the computational domain at $\Delta P_{ref} = 110$ mmHg.

$1.3 \cdot 10^6$ dyn/cm^2 and, as expected, the largest value occurs at the internal surface of the cylinder, where the radial displacement is higher. We observe that for Case 1 the Von Mises stress on the internal and external surfaces of the cylinder does not present a strong variability with respect to the constitutive model. This is related to the fact that the displacement field on the internal and external surfaces in Case 1 does not present a strong variability with respect to the constitutive model (as presented in Fig. 18), due to the calibration procedure described in Sec. 2.5. However, we report the dependency of the distribution of the Von Mises stress through the thickness of the vessel wall on the constitutive model, as presented in Fig. 24. In Case 2, represented in Figs. 23 and 25, the Von Mises stress presents a strong dependency on the constitutive model. More specifically, the different displacement fields in Figs. 19 result in the different pattern of the Von Mises stress, shown in Fig. 23. Fig. 25 indicates that for high levels of mechanical weakening, the variations of the Von Mises stress through the thickness of the vessel wall are strongly affected by the choice of the constitutive model. To conclude, Figs. 24 and 25 highlight the relevance of carefully choosing the constitutive model to represent the unhealthy arterial tissue.

5 Conclusions

In this paper we have addressed the numerical validation of isotropic and transversely isotropic models for the cerebral arterial tissue. The isotropic exponential type laws and the transversely isotropic models adequately fit the experimental data. The numerical results showed a good agreement with the data fitting; moreover, they highlighted the fact that isotropic models can be considered as a valuable option for the modeling of the arterial tissue when experimental observations of the directions of the collagen fibers in the tissue are not available. Afterwards we have analyzed the influence of the modeling choice for the unhealthy cerebral arterial tissue on the results of numerical simulations of static inflation tests. We have considered different levels of mechanical weakening of the vessel wall through a dimensionless weakening parameter D. The numerical simulations have shown that the choice of the type of constitutive model (i.e. isotropic or transversely isotropic) plays a key role in the spatial distribution of the mechanical stresses through the thickness of the vessel wall. This highligths the relevance of properly select the constitutive model when
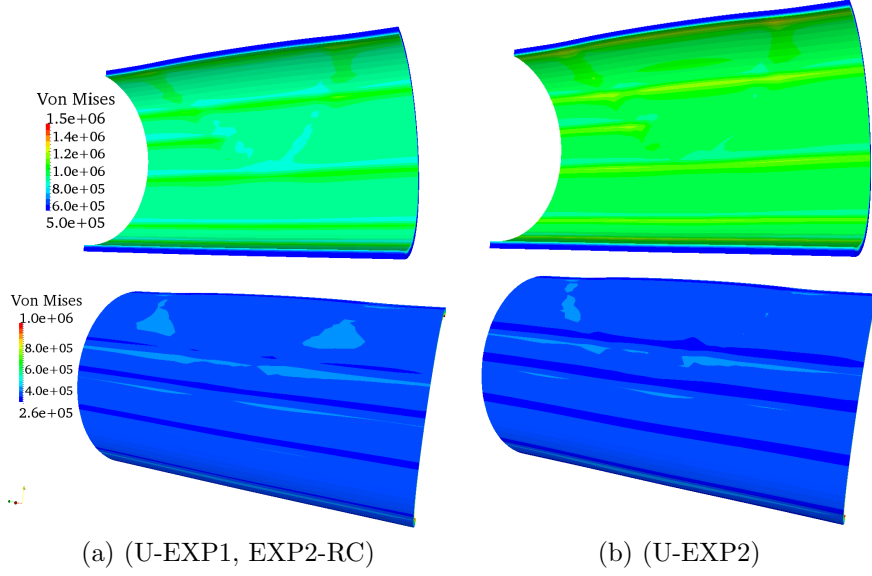
(a) (U-EXP1, EXP2-RC) (b) (U-EXP2)

Figure 23: Case 2: Von Mises stress field [dyn/cm^2] at the internal and external surfaces of the computational domain at $\Delta P_{ref} = 110$ mmHg.
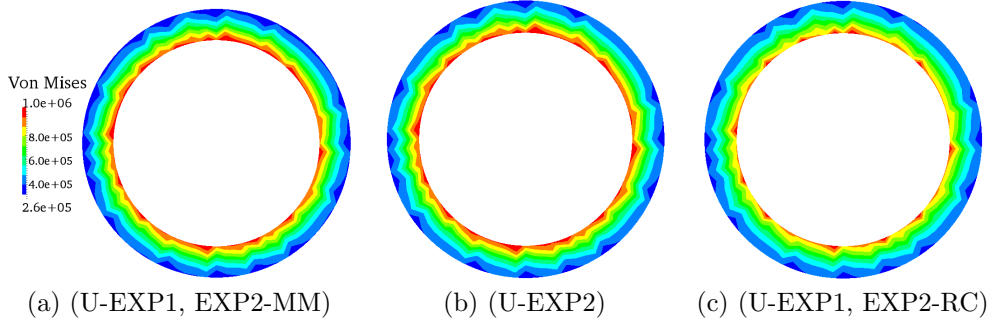

(a) (U-EXP1, EXP2-MM) (b) (U-EXP2) (c) (U-EXP1, EXP2-RC)

Figure 24: Case 1: Von Mises stress [dyn/cm^2] at $z = 1$ cm and $\Delta P = 110$ mmHg.

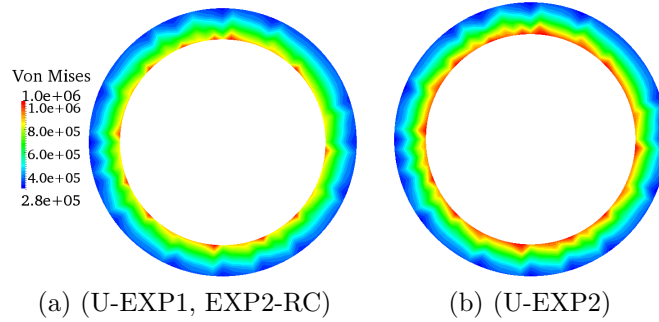(a) (U-EXP1, EXP2-RC) (b) (U-EXP2)

Figure 25: Case 2: Von Mises stress [dyn/cm^2] at $z = 1$ cm and $\Delta P = 110$ mmHg.

addressing the study of the onset and development of cerebral aneurysms. Concerning the transversely isotropic multi-mechanism model, specifically proposed for cerebral arteries, we have shown that it leads to the best approximation of the experimental measurements. Moreover, due to recruitment of the collagen

fibers at finite strains and the limited possibility of representing weakened states of the background material in arteries, the multi-mechanism model seems to be a valuable option for the mathematical description of the early stages development of cerebral aneurysm.

Acknowledgements

References

[1] Nichols W.W., O'Rourke M.F., *McDonald's blood flow in arteries: theoretical, experimental, and clinical principles.* London: Arnold, 1998.

[2] Holzapfel G.A., Gasser T.C., "A new constitutive framework for arterial wall mechanics and a comparative study of material models," *Journal of Elasticity*, vol. 61, pp. 1–48, 2000.

[3] Humphrey J.D., "Continuum Mechanics of soft biological tissues," *The Royal Society*, vol. 459, pp. 3–46, 2003.

[4] Burton A.C., "Relation of structure to function of the tissue of the wall of blood vessels." *Physiological Reviews*, vol. 34, pp. 619–642, 1954.

[5] Roach M.C., Burton A.C., "The reason for the shape of the distensibility curves of arteries." *Canadian Journal of Biochemistry*, vol. 35, pp. 681–690, 1957.

[6] Fung Y.C., *Biomechanics. Mechanical properties of living tissues.* New York: Springer, 1993.

[7] Humphrey J.D., *Cardiovascular Solid Mechanics. Cells, Tissues, and Organs.* New York: Springer-Verlag, 2002.

[8] Holzapfel G.A., *Nonlinear Solid Mechanics: a continuum approach for engineering.* England: John Wiley & Sons Ltd, 2000.

[9] Delfino A., Stergiopulos N., Moore J.E., Meister J.J., "Residual strain effects on the stress field in a thick wall finite element model of the human carotid bifurcation," *Journal of Biomechanics*, vol. 30, pp. 777–786, 1997.

[10] Torii R., Oshima M., Kobayashi T., Takagi K., Tezduyar T.E., "Fluid-structure interaction modeling of anuerysmal conditions with high and normal blood pressures," *Computational Mechanics*, vol. 43, pp. 151–159, 2006.

[11] Chen J., Wang S., Ding G., Yang X., Li H., "The effect of aneurismal-wall mechanical properties on patient-specific hemodynamic simulations: two clinical reports," *Acta Mechanica Sinica*, vol. 25, pp. 677–688, 2009.

[12] Valencia A., Burdiles P., Ignat M., Mura J., Bravo E., Rivera R., Sordo J., "Fluid structural analysis of human cerebral aneurysm using their own wall mechanical properties." *Computational and Mathematical Methods in Medicine*, vol. 2013, pp. 1–18, 2013.

[13] Bazilevs Y., Hsu M.C., Zhang Y., Wang W., Liang X., Kvamsdal T., Brekken R., Isaksen J.G., "A fully-coupled fluid-structure interaction simulation of cerebral aneurysms," *Comput Mech*, vol. 46, pp. 3–16, 2010.

[14] Isaksen J.G., Bazilevs Y., Kvamsdal T., Zhang Y., Kaspersen J.H., Waterloo K., Romner B., Ingebrigtsen T., "Determination of wall tension in cerebral artery aneurysms by numerical simulation." *Stroke*, vol. 39, pp. 3172–3178, 2008.

[15] Scott S., Ferguson G.G., Roach M.R., "Comparison of the elastic properties of human intracranial arteries and aneurysms," *Canadian Journal of Physiology and Pharmacology*, vol. 50, pp. 328–332, 1972.

[16] Spencer A.J.M., *Continuum Theory of the Mechanics of fibre-reinforced composites, CISM Courses and Lectures*. Wien: Springer-Verlag, 1984, ch. Constitutive theory of strongly anisotropic solids.

[17] Balzani D., Brinkhues S., Holzapfel G.A., "Constitutive framework for the modeling of damage in collagenous soft tissues with application to arterial walls," *Computer Methods in Applied Mechanics and Engineering*, vol. 1, pp. 139–151, 2012.

[18] Brands D., Klawonn A., Rheinbach O., Schröder J., "Modelling and convergence in arterial wall simulations using a FETI solution strategy," *Computer Methods in Biomechanics and Biomedical Engineering*, vol. 11, pp. 569–583, 2008.

[19] Calvo B., Pẽna E., Martinez M.A., Doblaré M., "An uncoupled directional damage model for fibred biological soft tissues. formulation and computational aspects," *International Journal for Numerical Methods in Engineering*, vol. 69, pp. 2036–2057, 2007.

[20] Gasser T.C., Holzapfel G.A., "Hyperelastic modelling of arterial layers with distributed collagen fiber orientations," *Journal of the Royal Society*, vol. 3, pp. 15–35, 2006.

[21] Dalong L., Robertson A.M., "A structural multi-mechanism constitutive equation for cerebral arterial tissue," *International Journal of Solids & Structures*, vol. 46, pp. 2920–2928, 2009.

[22] Wulandana R., Robertson A.M., "An inelastic multi-mechanism constitutive equation for cerebral arterial tissue," *Biomechanics and Modeling in Mechanobiology*, vol. 4, pp. 235–248, 2005.

[23] Kenneth L.M., Barbaro N.M., Manley G.T., "Biaxial response of passive human cerebral arteries," *Annals of Biomedical Engineering*, vol. 36, pp. 2028–2041, 2008.

[24] Sommer G., Regitnig P., Költringer L., Holzapfel G.A., "Biaxial mechanical properties of intact and layer-dissected human carotid arteries at physiological and supraphysiological loadings," *American Journal of Physiology. Heart and Circulatory Physiology*, vol. 298, pp. 898–912, 2010.

[25] Kamenskiy A.V., Dzenis Y.A., MacTaggart J.N., Lynch T.G., Kazmi S.A.J., Pipinos I.I., "Nonlinear mechanics behavior of the human common, external, and internal carotid arteries in vivo," *Journal of Surgical Research*, vol. 176, pp. 329–336, 2012.

[26] Flory P.J., "Thermodynamical relations for high elastic materials," *Transactions of the Faraday Society*, vol. 78, pp. 5222–5235, 1961.

[27] Odgen R.W., *Nonlinear elastic deformations*. New York: Courier Dover Publications, 1997.

[28] Sforza D.M., Putman C.M., Cebral J.R., "Hemodynamics of Cerebral Aneurysms," *Annual Review of Fluid Mechanics*, vol. 41, pp. 91–107, 2009.

[29] Wasserman S.M., "Adaptation of the endothelium to fluid flow: in vitro analyses of gene expression and in vivo implications." *Vascular Medicine*, vol. 9, pp. 34–45, 2004.

[30] Humphrey J.D., Canham P.B., "Structure, Mechanical Properties, and Mechanics of Intracranial Saccular Aneurysms," *Journal of Elasticy*, vol. 61, pp. 49–81, 2000.

[31] Sekhar L.N., Heros R.C., "Origin, growth and rupture of saccular aneurysms: a review." *Neurosurgery*, vol. 8, pp. 248–260, 1981.

[32] Austin G.M., Fisher S., Dickson D., Anderson D., Richardson S., "The significance of the extracellular matrix in intracranial aneurysms." *Annals of Clinical & Laboratory Science*, vol. 23, pp. 97–105, 1993.

[33] Ferguson G.G., "Physical factors in the initiation, growth, and rupture of human intracranial aneurysms." *Journal of Neurosurgery*, vol. 37, pp. 666–677, 1972.

[34] Campbell G.J., Roach M.R., "Fenestrations in the internal elastic lamina at bifurcations of the human cerebral arteries." *Stroke*, vol. 12, pp. 489–495, 1981.

[35] Humphrey J.D., Taylor C.A., "Intracranial and abdominal aortic aneurysms: similarities, differences, and need for a new class of computational models." *Annual Reviews of Biomedical Engineering*, vol. 10, pp. 221–246, 2008.

[36] Stehbens W.E., "Histopathology of cerebral aneurysms," *Archives of Neurology*, vol. 8, pp. 272–285, 1963.

[37] Kroon M., Holzapfel G.A., "A model for saccular cerebral aneurysm growth by collagen fibre remodelling." *Journal of Theoretical Biology*, vol. 4, pp. 775–787, 2007.

[38] Kachanov L.M., "Time of rupture process under creep conditions," *Izvestija Akademii Nauk Sojuza Sovetskich Socialisticeskich Respubliki (SSSR) Otdelenie Techniceskich Nauk (Moskra)*, vol. 8, pp. 26–31, 1958.

[39] Dalong L., "Structural multi-mechanism model with anisotropic damage for cerebral arterial tissues and its finite element modeling," Ph.D. dissertation, University of Pittsburgh, 2009.

[40] Carew T.E., Vaishnav R.N., Patel D.J., "Compressibility of the arterial wall," *CirculationRresearch*, vol. 23, pp. 61–68, 1968.

[41] Gasser T.C., Schulze Bauer C.A.J., Holzapfel G.A., "A three-dimensional finite element model for arterial clamping," *Journal of Biomechanical Engineering*, vol. 124, pp. 355–363, 2002.

[42] Nobile F., Pozzoli M., Vergara C., "Time accurate partitioned algorithms for the solution of fluid-structure interaction problems in haemodynamics," *Computer & Fluids*, vol. 86, pp. 470–492, 2013.

[43] Ball J.M., "Convexity conditions and existence theorems in nonlinear elasticity," *Archive for Rational Mechanics and Analysis*, vol. 63, 1977.

[44] Balzani D., "Polyconvex anisotropic energies and modeling of damage applied to arterial walls," Ph.D. dissertation, University of Duisburg-Essen, 2006.

[45] Simo J.C, Taylor R.L., "Quasi-incompressible finite elasticity in principal stretches. continuum basis and numerical algorithms," *Computer Methods in Applied Mechanics and Engineering*, vol. 85, pp. 273–310, 1991.

[46] Miehe C., "Aspects of the formulation and finite element implementation of large strain isotropic elasticity," *International Journal of Numerical Methods in Engineering*, vol. 37, pp. 1981–2004, 1994.

[47] Kroon M., Holzapfel G.A., "Estimation of the distributions of anisotropic, elastic properties and wall stresses of saccular aneurysms by inverse analysis," *Proceedings of the Royal Society A*, vol. 464, pp. 807–825, 2008.

[48] Raoult A., "Non-polyconvexity of the stored energy function of a Saint Venant-Kirchhoff material," *Applications of Mathematics*, vol. 31, pp. 417–419, 1986.

[49] Malossi A.C.I., "Partitioned solution of geometrical multiscale problems for the cardiovascular system: models, algorithms, and applications," Ph.D. dissertation, École Polytechinque Fédérale de Lausanne, 2012.

[50] Torii R., Oshima M., Kobayashi T., Takagi K., Tezduyar T.E., "Fluid–structure interaction modeling of a patient-specific cerebral aneurysm: influence of structural modeling," *Computational Mechanics*, vol. 38, pp. 482–490, 2008.

[51] Spencer A.J.M., *Theory of Invariants*.   Academic Press, 1971.

[52] Raoult A., "Symmetry groups in nonlinear elasticity: an exercise in vintage mathematics," *Communications on Pure and Applied Analysis*, vol. 8, pp. 435–456, 2009.

[53] Brinkhues S., Klawonn A., Rheinbach O., Schröder J., "Augmented Lagrange methods for quasi-incompressible material-Applications to soft biological tissue," *International Journal for Numerical Methods in Biomedical Engineering*, vol. 29, pp. 332–350, 2013.

[54] Quarteroni A., Sacco R., Saleri F., *Numerical Mathematics*.   Berlin Heidelberg: Springer, 2007.

[55] Naghdi P.M., Tang P.Y., "Large deformation possible in every isotropic elastic membrane," *Philosophical Transactions of the Royal Society A*, vol. 287, pp. 145–187, 1977.

[56] Naghdi P.M., "The theory of shells and plates," in *Handbuch der Physick. Mechanics of Solids*.   Berlin Heidelberg New York: Springer, 1984, vol. 2.

[57] Marquardt D., "An algorithm for Least-Squares estimation of nonlinear parameters," *SIAM - Journal on Applied Mathematics*, vol. 2, 1963.

[58] Brown A.M., "A step-by-step guide to nonlinear regression analysis of experimental data using microsoft Excel spreadsheet," *Computer Methods and Programs in Biomedicine*, vol. 65, pp. 191–200, 2001.

[59] Balzani D., Neff P., Schröder J., Holzapfel G.A., "A polyconvex framewok for soft biological tissues. adjustment to experimental data." *International Journal of Solids and Structures*, vol. 43, pp. 6052–6070, 2006.

[60] Tricerri P., "Mathematical and numerical modeling of cerebral aneurysm progression," Ph.D. dissertation, Instituto Superior Técnico and École Polytechinque Fédérale de Lausanne, In Preparation.

[61] Skrzypek J., Ganczarski A., *Modeling of material damage and failure of structures*.   Berlin Heidelberg: Springer-Verlag, 1999.

[62] Balzani D., Schöder J., Gross D., "Simulation of discontinuous damage incorporating residual stresses in circumferentially overstretched atherosclerosis arteries," *Acta Biomaterialia 2*, vol. 1, pp. 609–618, 2006.

[63] Quarteroni A., Valli A., *Numerical Approximation of Partial Differential Equations*.   Berlin Heidelberg: Springer-Verlag, 1999.

[64] Saad Y., *Iterative methods for sparse linear systems*.   Philadelphia: Siam, 2003.

[65] Quarteroni A., Valli A., *Domain Decomposition Methods for Partial Differential Equations*.   Oxford: Oxford University Press, 1999.

[66] *LifeV*, École Polytechnique Fédérale de Lausanne (CMCS), CH; Politecnico di Milano (MOX), ITA; INRIA (REO, ESTIME), FR, and Emory University (Math&CS), GA US., 2010, lifeV user manual, `http://lifev.org`.

[67] Quinodoz S., "Numerical simulations of orbitally shaken reactors," Ph.D. dissertation, École Polytechinque Fédérale de Lausanne, 2012.

[68] Hughes T.J.R., *The Finite Element Method: linear static and dynamic finite element analysis.* New York: Dover Publications, 2000.

MATHEMATICS INSTITUTE OF COMPUTATIONAL SCIENCE AND ENGINEERING
Section of Mathematics
Ecole Polytechnique Fédérale
CH-1015 Lausanne

27.2013   A. ABDULLE, G. VILMART, K. C. ZYGALAKIS:
High order numerical approximation of the invariant measure of ergodic SDEs

28.2013   S. ROSSI, T. LASSILA, R. RUIZ-BAIER, A. SEQUEIRA, A. QUARTERONI:
Thermodynamically consistent orthotropic activation model capturing ventricular systolic wall thickening in cardiac electromechanics

29.2013   F. BONIZZONI, F. NOBILE:
Perturbation analysis for the Darcy problem with log-normal permeability

30.2013   Z. LI, A. USCHMAJEW, S. ZHANG:
On convergence of the maximum block improvement method

31.2013   R. GRANAT, B. KAGSTRÖM, D. KRESSNER, M. SHAO:
Parallel library software for the multishift QR algorithm with aggressive early deflation

32.2013   P. CHEN, A. QUARTERONI:
Weighted reduced basis method for stochastic optimal control problems with elliptic PDE contstraint

33.2013   P. CHEN, A. QUARTERONI, G. ROZZA:
Multilevel and weighted reduced basis method for stochastic optimal control problems constrained by Stokes equations

34.2013   A. ABDULLE, M. J. GROTE, C. STOHRER:
Finite element heterogeneous multiscale method for the wave equation: long time effects

35.2013   A. CHKIFA, A. COHEN, G. MIGLIORATI, F. NOBILE, R. TEMPONE:
Discrete least squares polynomial approximation with random evaluations-application to parametric and stochastic elliptic PDEs

36.2013   N. GUGLIELMI, D. KRESSNER, C. LUBICH:
Computing extremal points of symplectic pseudospectra and solving symplectic matrix nearness problems

37.2013   S. DEPARIS, D. FORTI, A. QUARTERONI:
A rescaled localized radial basis functions interpolation on non-cartesian and non-conforming grids

38.2013   A. GIZZI, R. RUIZ-BAIER, S. ROSSI, A. LAADHARI, C. CHERUBINI, S. FILIPPI:
A three-dimensional continuum model of active contraction in single cardiomyocytes

39.2013   P. TRICERRI, L. DEDÈ, A. QUARTERONI, A. SEQUEIRA:
Numerical validation of isotropic and transversely isotropic constitutive models for healthy and unhealthy cerebral arterial tissues